Structural Connectivity and White Matter Health in Adults Born Very Low Birthweight

L.W. Bignell

July 16, 2022

Abstract

Children born very preterm or with a very low birthweight (VLBW), are at a significantly elevated risk of brain injury from inflammation or hypoxic-ischaemic events. Resulting damage to pre-myelinating cells and other issues, commonly lead to diffuse and acute white matter injury with long term impacts on cognitive and motor function. On average, over one in ten births are now preterm. Mortality rates for preterm births have declined, but unfortunately, neurological disorders remain a major impairment for this group.

The New Zealand VLBW cohort enrolled all infants born VLBW in 1986, and has undergone several multi-disciplinary follow up studies. Most recently, this included comprehensive cranial MRI scans at an age between 26 and 30 years. The MRI session included diffusion-weighted imaging, to examine white matter health in early adulthood. Probabilistic tractography has been used to isolate whole white matter tracts and to construct structural networks.

Of the 42 tracts identified, 12 showed significantly reduced volumes in the VLBW cohort (n = 141) compared to controls born normal birthweight (n = 49). These included the acoustic radiations, left cortico-spinal tract, left superior thalamic radiation, forceps major and minor, and the inferior longitudinal fasciculi. This indicates that the impact of an early birth remains as smaller WM volumes in early adulthood. Only three tracts showed altered diffusion properties. The forceps major and left temporal cingulum subsection showed a reduction in fractional anisotropy; these two tracts, along with the right optic radiation, also show an increase in radial diffusivity. These diffusion properties indicate poorer white matter health for these tracts, but this is much less pronounced than is commonly reported in child and adolescent studies. Taken together, these results suggest that the white matter of VLBW individuals may eventually mature similarly to their term born peers, but with lasting reductions in volume.

Structural network analysis used: AAL3 parcellation; FSL's probabilistic tractography; and two normalisations, a standard approach (waytotal) and a novel algorithm developed for this thesis (node strength normalisation). This analysis found the VLBW group had marginally increased global efficiency, with an unchanged characteristic path length, suggesting that the short paths may be shorter in the VLBW group. Mean clustering coefficient was significantly decreased, and node-wise clustering generally reflected this trend. Notably, the cerebellum showed a slightly higher clustering in the VLBW group potentially in relating to impaired motor function. Modularity was higher, indicating a stronger community structure in the scale of 20-40 nodes.

This thesis also introduced a novel normalisation algorithm: node strength normalisation (NSN). This algorithm allows nodes to have their strengths estimated and scaled relative to each other, allowing meaningful comparisons between subjects, with minimal underlying assumptions. It is the hope that NSN will be applicable more broadly, improving the validity of structural network analyses across a wide range of neuroimaging applications.

Contents

List of acronyms

AAL	Automated anatomical labelling
AD	Axial diffusivity
ADHD	Attention deficit hyperactivity disorder
ASD	Autism spectrum disorder
BCT	Brain connectivity toolbox
BOLD	Blood oxygenation level dependent
CC	Clustering coefficient
CP	Cerebral palsy
DTI	Diffusion tensor imaging
DWI	Diffusion weighted imaging
EEG	Electroencephalogram
FA	Fractional anisotropy
FDR	False discovery rate
fMRI	functional MRI
FSL	FMRIB Software Library
FT	Full term
GM	Gray matter
IVH	intra-ventricular haemorrhage
MD	Mean diffusivity
MEG	Magnetoencephalography
MNI	Montreal Neurological Institute
MRI	Magnetic resonance imaging
MSE	Mean squared error
NICU	Neonatal intensive care unit
NoS	Number of streamlines
NSN	Node strength normalisation
NZ	New Zealand
PC	Principal component
PCA	Principal component analysis
PVL	Periventricular leukomalacia
RC	Rich club
ROI	Region of interest
TBSS	Tract based spatial statistics
VLBW	Very low birth weight
VP	Very preterm
WM	White matter

1 Introduction

1.1 Preterm births

Human gestation is rapid and complex. When development is interrupted by a premature birth, it can have long-term health consequences [Cai et al., 2019, Evensen et al., 2020, Patel, 2016]. This forms the basis of the Developmental Origins of Health and Disease Theory [Wadhwa et al., 2009], which postulates that individuals can be predisposed to several health disorders throughout their lifetime as a result of environmental influences at critical stages of fetal and early child development [Mandy and Nyirenda, 2018, Arima and Fukuoka, 2020]. This theory is supported by the increased rates of neurological and cognitive disorders, respiratory issues, blindness and deafness associated with preterm births [Ward and Beachy, 2003, Su et al., 2016].

A typical pregnancy lasts around 37 to 42 weeks, with a healthy birthweight around 2500g to 4500g [ICD, 2019]. One in ten pregnancies however, result in premature birth (<37 weeks gestation) [Chawanpaiboon et al., 2019, Vogel et al., 2018]. Survival rates have dramatically improved with medical advancements, such that most premature infants with access to high quality neonatal care are expected to survive to adulthood. However, with the threshold of viability now at approximately 23 weeks gestation, the short-term and long-term morbidity of preterm birth places a significant burden on individuals, families and health-care systems [Rogers and Hintz, 2016]. Understanding the effect of the developmental disruption associated with preterm birth is important to help guide interventions to improve patient outcomes.

Both gestation time and birthweight are indicators of prenatal development, which have been used in the study of neonatal outcomes, although they are not exactly equivalent [Hollanders et al., 2019]. Historically, birthweight was seen to be the more reliable indicator, however this has moved toward gestational age with the development of ultrasound in recent years. Specific definitions of very-preterm (VP; generally <32 weeks gestation) and very low birthweight (VLBW, birthweight <1500g) vary between studies and regions. The criterion used for this study was a birthweight under 1500g, standard for 1986 when the study commenced.

Morbidities

The neurocognitive morbidities more commonly observed in VLBW/VP born individuals fall across several domains. These include sensory-motor, social cognition and executive function. Though many studies are focused on the early years of development, it is important to note that many of these issues persist beyond childhood, and cause lifelong difficulties.

Movement and coordination disorders affect approximately 37% of VP individuals in childhood [Bolk et al., 2018,Arnaud et al., 2007]. Cerebral palsy (CP) affects around 10% of individuals born less than 28 weeks [Himpens et al., 2008, Smith et al., 2020]. These movement disorders vary in severity, from awkwardness walking and moving, to requiring special equipment, or an inability to move independently at all.

Attention problems, processing speeds and attention deficit hyperactivity disorder (ADHD) are seen at much higher rates in VLBW/VP cohorts throughout childhood [Agrawal et al., 2018,Franz et al., 2018,Alamolhoda et al., 2021]. These problems are found to negatively correlate with school achievement and IQ, and to persist into adulthood [Jaekel et al., 2013,Robinson et al., 2022, Breeman et al., 2016]. Working memory impairments are also found, which relate to lower

IQ observed in VLBW/VP individuals [Ward and Beachy, 2003, Kelly et al., , Dong and Yu, 2011]. This impacts these individuals throughout their lives, influencing their schooling success and career prospects.

Other neurological issues include autism spectrum disorder (ASD) and epilepsy. ASD has been found to affect around 7% of VP/VLBW individuals, impacting on their quality of life in a variety of ways, including lower rates of social engagement, higher rates of underemployment and mental health problems [Agrawal et al., 2018, Limperopoulos et al., 2008, Stephens et al., 2012] Epilepsy is observed at greatly increased rates (around 4.5 times) in preterm children and adults compared to full-term, with risk decreasing with increased gestational age [Hirvonen et al., 2017, Crump et al., 2011].

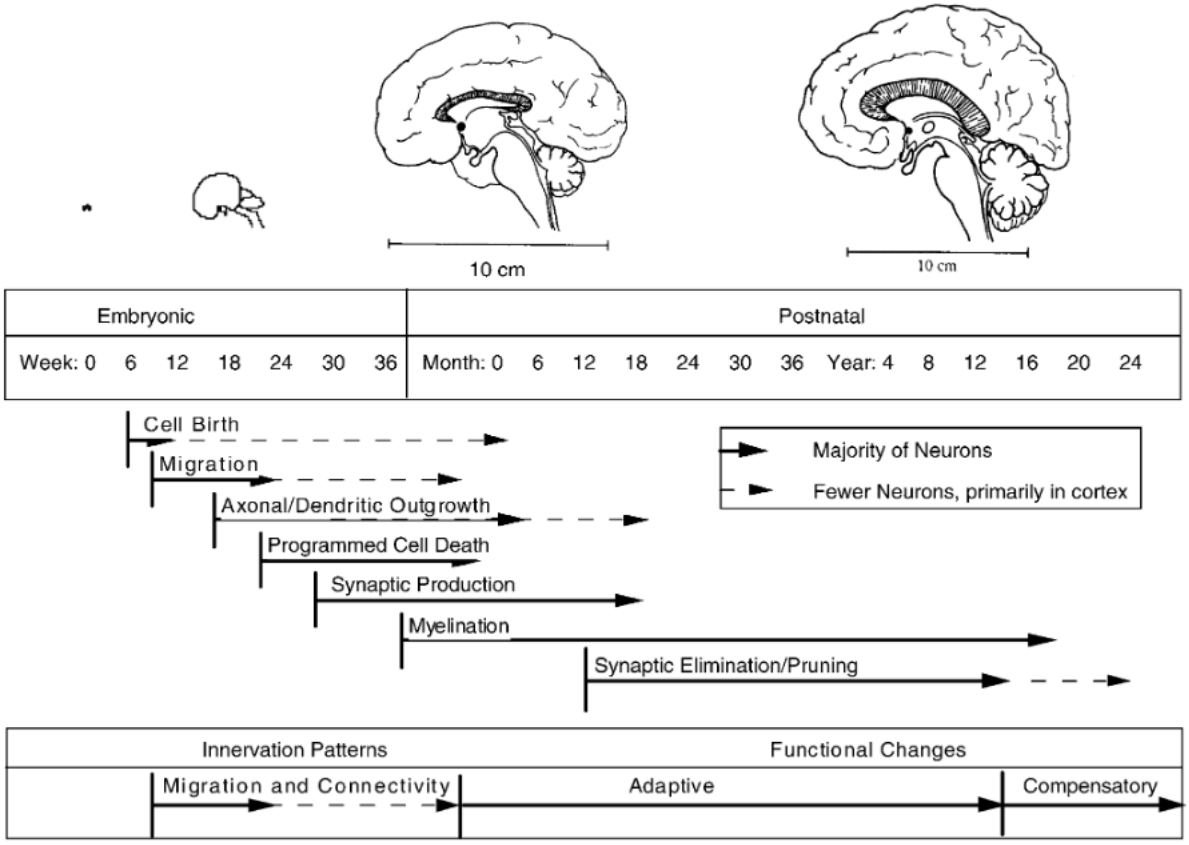

Figure 1: Early brain development timeline.
Reprinted from Neuroscience & Biobehavioral Reviews , Volume 27, Issues 12, Susan L Andersen, Trajectories of brain development: point of vulnerability or window of opportunity?, Pages 3-18, Copyright 2003, with permission from Elsevier

Processes underlying common morbidities

VLBW/VP neonates are not ready for the unfavourable environment outside the womb. The ideal in-utero environment provides a stable, continuous supply of oxygen and nutrients through the placenta, and protects the fetus with a stable temperature, low light, low noise environment free of infection, inflammation and injury. By contrast, a preterm birth is often preceded by a suboptimal in-utero environment, where energy or oxygen supply may be impaired, or the fetus is exposed to infection and inflammation. This is followed by the experience of the NICU, which exposes the neonate to light, noise, variable temperatures, microbes, excess oxygen and more. This forces immature organs, such as the immune and respiratory organs, to quickly adapt to function in the post-natal environment cite.....

Particularly important is the vulnerability of the developing brain to ischemia, inflammation, and infection. These factors are known to commonly lead to acute and diffuse injury.

On the cellular level, the neurological development ongoing during an early birth includes synapse production, myelination and refinement of the connectivity structure through neuron and axonal growth and migration, and programmed cell death (roughly outlined in figure 1). At this stage the surface of the cortex is largely smooth, with the surface gray matter (GM) rapidly proliferating and beginning to fold. The connections within the brain are taking shape, with the white matter (WM) tracts being established, and myelination beginning [Kocak, 2009, Poduslo and Jang, 1984].

Myelination is the process of wrapping axons in a fatty, insulating sheath, which enables rapid and efficient electrical communication along axons. Some structures are normally myelinated at term, but most myelination occurs in the first two years post-birth [Grant and Griffin, 2018]. The cells which go on to perform myelination are pre-myelinating oligodendrocytes (preOLs). PreOLs are particularly vulnerable to hypoxia-ischemia and inflammation events, due to their immaturity, and so are at a high risk of death or harm in VLBW/VP neonates. Death of these preOLs causes rapid growth and specialisation of their precursor cells, but the regenerated preOLs, and those injured are poorer myelinators, ultimately leading to a widespread white matter injury (WMI). Neurons are also affected in hypoxia-ischemia events, with a widespread impact on to dendritic growth, and general GM atrophy observed [Back, 2014, Volpe, 2009].

The delicate blood vessels in the preterm brain are also particularly vulnerable to disruption, and at a high risk of rupturing. Intraventricular hemorrhaging (IVH), bleeding into the ventricles, is an occurance of this which significantly damages tissues adjacent to the ventricles in 10-15% of VLBW individuals [McCrea and Ment, 2008, Ballabh and de Vries, 2021].

Damage to the deep white matter near the ventricles, periventricular leukomalacia (PVL) can also result from adverse events in the NICU, and affects from a fifth to half of VLBW/VP individuals [Volpe, 2008b, Collins et al., 2018, Volpe, 2008a].

These disruptions have a widespread effect on both WM and GM health, and are consistent with the morbidities mentioned above [Shah et al., 2008, Murray et al., 2014]. White matter injury can account for the majority of neurological deficits [Khwaja and Volpe, 2008]. Further, white matter injury is found to mediate aspects of GM development and abnormal neurodevelopment [Shah et al., 2008, Murray et al., 2014].

MRI studies of neonates and infants have been used to quantify the location and severity of this disrupted growth [Kidokoro et al., 2013, Edgin et al., 2008]. These disruptions are found throughout the newborn VLBW/VP brain, due to the diffuse nature of the injuries. With a sim-

ilarly wide range of neurocognitive impairments, it is difficult to identify specific regions relating to adverse outcomes. A review of the relationship between WM tracts and childhood disorders highlighted the corpus callosum, cerebellum, centrum semiovale, sensorimotor, subcortical nuclei, and posterior limb of the internal capsule as frequently being found with reduced volumes in VLBW/VP cohorts [Parikh, 2016].

Studies through childhood and adolescence again find a broad range of structural alterations throughout the brain, frequently related to patient outcomes. Volumetric studies of WM tracts often highlight the corpus callosum, internal and external capsules, cerebellum and spinal chord [Gimnez et al., 2006, Soria-Pastor et al., 2008, Taylor et al., 2011, Cald et al., 2006], with particularly poor outcomes for patients who experienced IVH [Nosarti et al., 2008]. Diffusion tensor imaging (DTI; see section 1.2) studies of WM health indicate impaired WM health in VLBW/VP groups, in addition to reduced volumes. These studies also highlight the internal and external capsule, corpus callosum, especially the splenium, in addition to the left and right uncinate fasciculi, and many other WM tracts [Eikenes et al., 2011,Constable et al., 2008,Skranes et al., 2007, Mullen et al., 2011, Vollmer et al., 2017]. Largely WM health is inferred through a reduction in fractional anisotropy (FA), often with a corresponding increase in mean diffusivity. These measures are explored in section 1.2.

Imaging studies of adults born VLBW/VP are very few. A study on hippocampal structure found reduced volme in VLBW adults at age 26 [Aanes et al., 2020]. A previous study of this dataset on GM thickness found atrophy in medial and lateral temporal areas in the VLBW group, which also correlated with attention [Pascoe et al., 2019].

As individuals born preterm or with very low birthweight progress into adulthood, as with everyone, their brain matures and adapts. The extreme plasticity of the developing brain may allow some amount of the damage to be repaired or appropriate and efficient compensatory pathways to be established. To properly assess this, and to understand the trajectory of abnormal brain development, studies of VLBW/VP individuals need to be done later in life as well. These studies are relatively few, and it is the aim of this thesis to add to the sparse literature on VLBW brain development into early adulthood. Considering the important impairments to white matter development, and the strong relationship between cognitive outcomes and WM integrity and volume, this thesis will focus on WM health in the brains of adults born VLBW.

1.2 Magnetic resonance imaging

Magnetic resonance imaging (MRI) is an astoundingly flexible 3D imaging technique. MRI is non-invasive, non-ionising with excellent soft tissue contrast. MRI also has a great variety of scanning protocols which allow for different characteristics to be measured, such as T1 and T2 structural images, arterial spin labelling and most importantly here, diffusion weighted imaging (DWI). Its excellent contrast, flexibility, and non-invasiveness lend it to be used in brain research for both children and adults.

MRI is based on the behaviour of atomic nuclei, typically hydrogen, in a strong magnetic field ($\vec{B_0}$). Classically, the magnetic moments of the hydrogen nuclei generally align with the external magnetic field. These nuclei may be excited by a resonant radio pulse, which rotates the nuclei away from (or toward) aligning with $\vec{B_0}$. Nuclei precess around $\vec{B_0}$ as per the larmor equation $\omega = \gamma B_0$, where omega is the angular velocity of the precession and γ is the gyromagnetic ratio.

When precessing together this ensemble emits a detectable radio wave. Contrast in MRI comes from differing net transverse magnetic moments specific to different tissues, resulting from either re-alignment of the nuclei with $\vec{B_0}$ (T1), or an (irreversible) lack of cohesion in the ensemble precession (T2).

Diffusion

Diffusion in the brain is strongly influenced by underlying microstructure. In areas with loose, non-ordered microstructures, such as the ventricles, movement of water is largely unobstructed. This results in large, undirected (ie. isotropic) diffusion. By contrast, GM has a relatively restrictive, but generally isotropic microstructure, resulting in weak undirected diffusion. WM tracts are most interesting: the highly ordered, tube-like structure of axons cause moderate-high diffusion parallel to the tracts, but very low diffusion perpendicular. For this reason, the ability of diffusion imaging to quantify how water movement is impeded allows for informative inferences on the health, strength and directionality of the underlying micro-structure [Alexander et al., 2007].

Diffusion weighted imaging

Diffusion-weighted imaging (DWI) is a scanning protocol which is sensitive to diffusion (of water). In essence, DWI tags water in a small volume, then records the proportion which remains in that volume after a short interval. Each scan is parametrised by a b-vector ($\vec{b}$), which gives the direction of diffusion sensitivity, and a b-value (b, s/mm^2) which relates to the magnitude of the sensitivity. Acquiring many DWIs with at least two b-values (usually several with $b = 0$), allows analysis of diffusion properties, which may be used to make inferences about the underlying microstructure.

To achieve sensitivity to diffusion, a gradient magnetic field (along $\vec{b}$) is applied, followed by a reverse gradient a short time later (generally 20-50 ms). The gradient field causes a change in precession speed, de-phasing the precession along $\vec{b}$ by an angle which is functionally dependant on position in the $\vec{b}$ direction. The negative gradient then attempts to re-phase the precession at each point/plane, by applying an equal and opposite gradient, such that precession at any point along $\vec{b}$ is rotated back by the same angle. Any particles which have moved along $\vec{b}$ between gradient applications will experience a different change in phase, and so have their phase scattered. This loss of phase coherence causes a drop in signal proportional to diffusion along $\vec{b}$. By comparing this image to one with no (or different) diffusion weighting, diffusion can be quantified under a variety of models, producing images such as figure: 2 [Mori and Zhang, 2006].

Modern DWI sequences can collect hundreds of whole brain images: one for each of a few b-values, for each of potentially hundreds of b-vectors. The volume of data produced necessitates further processing (beyond the usual artefact reduction etc); common approaches to quantifying diffusion include DTI, diffusion kurtosis imaging, neurite orientation dispersion and density imaging, and constrained spherical deconvolution.

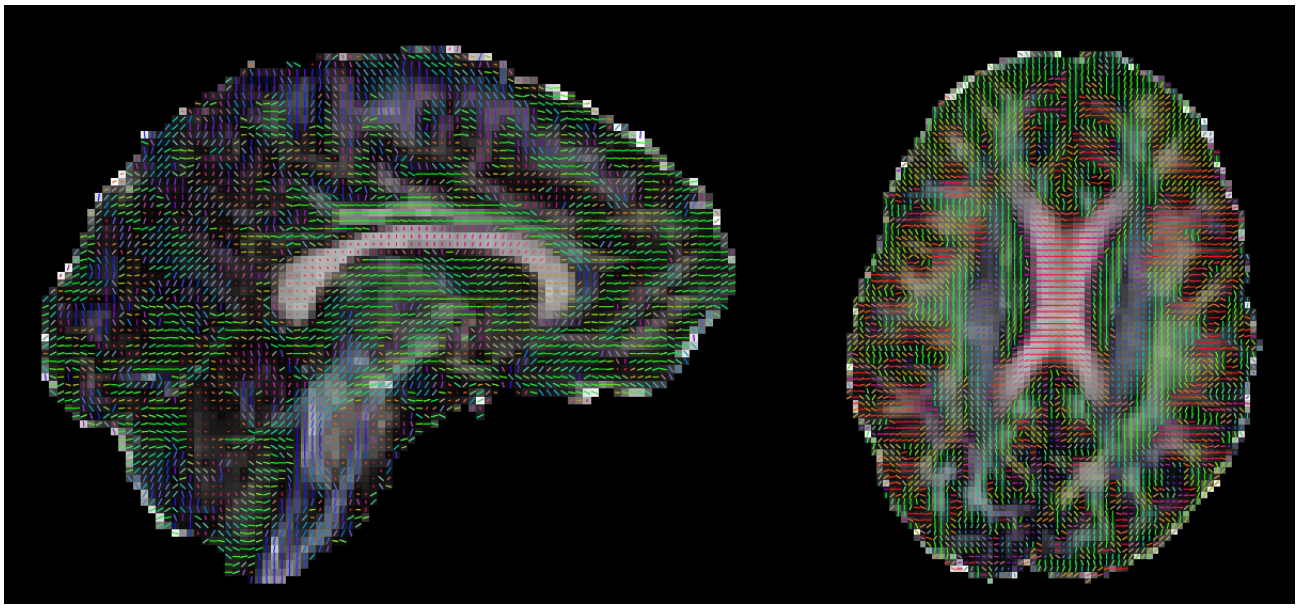

Figure 2: Diffusion tensor image, showing FA in grayscale, with coloured lines overlayed showing direction of primary diffusion. Blue: inferior-superior; green: anterior-posterior; and red: left-right. WM is seen in white, as it has a high FA. Visible WM tracts include: the corpus callosum (red), seen as a central frown in the para-sagittal view (left) and a central cross in the transverse view (right), with diffusion running left-right; and the cingulum bundle running anterior-posterior (green), following the superior edge of the corpus callosum in the para-sagittal view.

Diffusion tensor imaging

Diffusion tensor imaging (DTI) is perhaps the most established method for processing DWIs. DTI makes the strong assumption that each voxel contains homogeneous tissue in which diffusion occurs as a multivariate gaussian. As such, observed differences can have a variety of underlying causes, making interpretation difficult. A brief overview of DTI and the subsequent metrics used in this analysis is provided here.

DTI represents diffusion with a 'diffusion ellipsoid' at each voxel. This estimates the average diffusion in each direction as the radius of the ellipsoid in said direction. The ellipsoid can be represented by a 3x3 matrix D, though commonly this is broken into its eigenvalues and rotations to the respective eigenvectors, giving: $D = V\Lambda V^T$ with

$$\Lambda = \begin{bmatrix} \lambda_1 & 0 & 0 \\ 0 & \lambda_2 & 0 \\ 0 & 0 & \lambda_3 \end{bmatrix}$$

The shape and size of these ellipsoids are characterised by the eigenvalues, which are commonly analysed with the following metrics:

Fractional anisotropy (FA) quantifies how directional a diffusion signal is. FA is calculated as

$$FA = \sqrt{\frac{(\lambda_1 - \lambda_2)^2 + (\lambda_2 - \lambda_3)^2 + (\lambda_3 - \lambda_1)^2}{2({\lambda_1}^2 + {\lambda_2}^2 + {\lambda_3}^2)}} \tag{1}$$

This gives FA a value between 0 (undirected/isotropic diffusion) and 1 (diffusion in a single direction only). An example DTI construction is figure 2, which highlights WM tracts by their high FA.

Mean diffusivity (MD) quantifies the overall magnitude of the diffusion. MD is calculated as the mean of the eigenvalues,

$$MD = \frac{\lambda_1 + \lambda_2 + \lambda_3}{3} \tag{2}$$

Other common metrics include axial diffusivity (AD = λ_1), which quantifies the magnitude of the diffusion along the direction of greatest diffusion, and radial diffusivity (RD = $(\lambda_2 + \lambda_3)/2$) which quantifies diffusion perpendicular to primary diffusion. Interpretation of these is more nuanced, and can in part be inferred by FA and MD, so have been excluded from this analysis.

Interpretations of DTI metrics

A great amount of work has gone into characterising what, and how microstructural configurations affect these metrics. In specific circumstances, they can be highly informative, but care must be taken when interpreting them; several arrangements of complex architecture can give rise to similar summary metrics.

Intracellular elements are deemed unimportant when explaining diffusion properties. Studies on the giant axons of the squid and lamprey have allowed the axoplasm to be imaged isolated from the cell membranes in a living axon. These found very low FA (0.11 and 0) and an MD similar to that of water (71% and 72%) [Beaulieu and Allen, 1994, Takahashi et al., 2002].

The cell membrane has been found to be the main contributor to FA. This has been confirmed through studies of various unmyelinated WM tracts. These include: normally unmyelinated WM [Beaulieu, 2002, Takahashi et al., 2002], WM which has not yet undergone myelination (neonatal studies) [Partridge et al., 2004, Larvaron et al., 2007], and where pathology prevents WM myelination [Harsan et al., 2007, Tyszka et al., 2006]. These studies each found a significant degree of FA (0.2 to 0.8 depending on species and tract) indicating that the bulk of FA comes from the axon cell membrane.

Myelination is thought to play an influencing role on FA, but to be a smaller contributor relative to cell membrane integrity. Comparisons between the above unmyelinated fibres and their appropriate myelinated counterparts found the myelinated fibres to have an FA 12% to 40% greater, and also an MD almost always reduced by 10% - 20% [Harsan et al., 2007, Tyszka et al., 2006].

This indicates that DTI should be a good indicator of WM health, however care needs to be taken to maintain specificity. Various artefacts are commonly seen when the assumptions of DTI are not met. Partial volume effects with CSF near the ventricles artificially lower FA and increase MD. The presence of multiple fibre bundles, such as at the crossing of the Corpus callosum and corticospinal tract, also reduces FA, and flattens the tensor. Recent studies with multiple b-values have also determined the diffusion to be non-gaussian in time, and newer methods such as diffusion kurtosis imaging have been established to account for this.

A study on Wallerian degeneration along the motor pathways found decreased FA when the tracts were isolated, but unchanged where they crossed other tracts [Pierpaoli et al., 2001]. A reduction in RD with similar AD was linked to dysmyelination without axonal damage [Song

et al., 2002], however many arangements of fibre populations were found which could give rise to this change [Wheeler-Kingshott and Cercignani, 2009, Douaud et al., 2009].

Tractography

Another way to utilise DWIs is through tractography. WM tracts are of course not localised to individual voxels, but appear as a series of adjacent, similarly aligned voxels throughout a diffusion image. These may be followed producing a streamline along a particular WM pathway.

Different techniques have been developed to carry out this procedure, based on how each voxel's diffusion is modelled. Older deterministic algorithms have been replaced by increasingly sophisticated probabilistic methods. In the determinnistic approach, the direction of greatest diffusion is followed every time. The probabilistic approach used in this thesis is the ball and stick model. In this model, each voxel contains a number of infinitely anisotropic components, representing WM fibre populations, and an isotropic component, representing noise and scattered fibres. As a streamline reaches each voxel, a random direction from that voxel's modelled fibre distribution can be drawn and followed. Each technique has advantages and disadvantages; the probabilistic model was chosen here as it is robust to uncertainty in the diffusion measurements.

This is further explored in section 2.5

1.3 Methods of analysis

Multiple techniques exist to analyse whole brain images. Specifically for DWI, two main avenues stand out: tract-, or region-wise analysis; and network analysis.

The region-of-interest approach entails identifying regions (WM tracts) in each subject, and extracting summary metrics such as FA or MD. The gold standard for identifying WM tracts is expert manual segmentation, however this is laborious, and impractical for large datasets. A whole brain approach like tract based spatial statistics (TBSS), which has been previously used on this dataset, is a method which registers the highest FA from voxels perpendicular to a pre-specified WM skeleton [Pascoe et al., 2019]. This picks out the centre of WM tracts, but loses information from the tract as a whole, as each voxel forms its own comparison, loses statistical power, as more stringent multiple comparisons control is needed, and it can be difficult to account for partial volume effects. TBSS is also limited in that it cannot determine the volume of tracts. Tractography may be used with pre-specified masks designed to isolate whole WM pathways in each subject, as seen in figure 3. This allows the whole tract to be isolated, and analysis done on a tract-by-tract basis. This increases statistical power, captures all voxels within the length and breadth of a tract, and allows for volumetric analysis.

The second, fundamentally different approach is to treat the brain as a network (a mathematical graph). This approach defines regions of GM, and focuses on the connections between them, as opposed to summary metrics from the regions themselves. For this analysis, tractography is run between each pair of regions. The number of streamlines then indicates the strength of that connection.

Both types of analyses can tell us something about the brain and the state of WM. In this thesis both techniques are explored in an effort to provide a more complete picture of the state of the adult brain born VLBW.

1.4 Network analysis

It almost goes without saying that the brain is a network by nature. This structure exists as a fractal, from the molecular biochemistry in the scale of angstroms to the incorporation of peripheral nerves on the scale of metres [Sejnowski, 2016]. A network in this context is a mathematical graph representing connectedness within the brain. This graph is a set of nodes (or vertices), along with a matrix of edges, representing how the nodes are integrated. These networks can vary greatly in construction and interpretation based on the scale and imaging modality used.

Micro- and meso- scale networks

On the cellular level, individual neurons can form the nodes of this network, connected via a multitude of synapses. Estimates of the number of neurons present in a human brain are in the order of 10^{11}, with 10^{15} synapses between them [Herculano-Houzel, 2009]. In addition to where these connections are, information on the type and strength of these connections is important to understanding how they function [Sporns et al., 2005]. Whilst such a description would provide profound insight, the level of detail required exceeds our capacity to efficiently collect, store, and process such data [Mikula, 2016].

On the slightly larger 'mesoscale,' structures may be seen in the local groupings of neurons. Groups of around 10-100 cells form cortical columns and mini-columns, tiny units perforating the neocortex [Cruz et al., 2005]. There is some evidence that these form functional units in the brain, making a network of this scale highly attractive [Jones, 2000, Buxhoeveden and Casanova, 2002]. With a width of around 40-80 μm, mapping these still presents a colossal task, and falls well below what may be studied in vivo.

Macroscale networks

This begs the question: what *can* we measure? The tools of modern, non-invasive network analysis are generally limited to electro- and magneto-encephalography (EEG and MEG); and functional and diffusion magnetic resonance imaging (MRI) [He and Evans, 2010]. These modalities can reach resolutions down to millimetres, as such they are considered 'macro-scale' networks [Hedrich et al., 2017]. EEG, MEG and functional MRI (fMRI) all seek to measure activity in the brain, through electrical or magnetic signals (EEG and MEG) or changes in magnetic susceptibility resulting from increased blood flow (fMRI, in particular blood oxygen level dependent imaging (BOLD)). Diffusion MRI seeks to map WM pathways, by characterising the diffusion of water within the brain. Diffusion MRI is the technique used in this analysis, and so will be explained in slightly more depth in the following sections.

Ionising modalities such as positron emission tomography and single-photon emission computed tomography are also able to produce informative functional images, such as by measuring glucose metabolism or cerebral blood flow. These techniques require the injection of radionuclides, which will expose participants to a small degree of harmful radiation. As such, a more thorough cost-benefit analysis is needed to justify their use.

Parcellation

Defining the nodes of a network (parcellation) is a matter of active research, and depends greatly on the imaging modality used. EEG and MEG are the simplest, as each electrode or magnetometer quite naturally lends itself to be used as a node ([Bosma et al., 2009] for example). Some variability exists, depending on the headcap or MEG machine used, but for a given study, node choice is generally straightforward. In MRI, 3d images are produced without externally defined nodes, which leaves node construction a much more open problem. In general, voxels are grouped or parcellated into regions of interest (ROIs) either randomly (with some constraints) or based on a priori anatomical and/or functional information.

Each Node should be a homogeneous region, sharing similar connections and function(s). Function, information processing and task performing in the brain, is carried out by the grey matter (GM) residing mainly on the cortical surface. White matter (WM) conducts signals between GM volumes, and as such, will be involved in the construction of the edges. Ideally then, parcellations should consist exclusively of distinct GM regions [Park and Friston, 2013]. Many templates exist which have been expertly constructed to divide the brain into known anatomical and/or functional regions [Zalesky et al., 2010, Rolls et al., 2020, Destrieux et al., 2010]. Another approach is to extract the GM and randomly parcellate it into similarly sized, contiguous regions. With small enough regions, these should achieve the desired result, though interpretations will differ. Anatomical pacellations are generally limited to fewer than 150 ROIs, but random parcellations may push this in excess of 5000 [Qi et al., 2015].

No gold standard currently exists for parcellations; it is an open question to what degree parcellation affects network measures [Qi et al., 2015, Zalesky et al., 2010, Wang et al., 2011]. This is a very interesting question, but falls beyond the scope of this thesis.

Edge construction

The construction of the edges of a network is where the main distinction between functional and structural networks lies. EEG, MEG and fMRI produce time series data of brain activity. The strength of the edge between each pair of nodes in functional networks is based on the correlation in this activity time series. This lends toward the interpretation of connected regions being strongly involved in performing the same task(s) [van den Heuvel et al., 2017, van Diessen et al., 2015]. Diffusion MRI on the other hand, produces data on how water diffuses throughout the brain (further explained in 1.2). With this, WM tracts may be traced, following the process of tractography (further explained in 2.5) from each ROI to each other ROI. The edge strength will be related to the number of streamlines which connect each pair of ROIs. This lends the edges to be interpreted as the strength of the physical connection between regions, which may be involved in information transfer, or capacity for functional integration.

Usefulness of macroscale networks

With such a coarse representation of the underlying networks, one may wonder whether meaningful inferences can be gleaned from macro-scale networks. With each voxel containing $\sim 10^5$ neurons [Cosgrove et al., 2007, Herculano-Houzel, 2009], these networks alone will not reveal the arcane workings of the mind. They do however show some robust properties, with disruptions commonly seen in certain neurological disorders. Some of these are mentioned here to further motivate and justify analysis of these networks, and give examples of metrics used.

Metric selection and explanation are the subject of section 2.7.4, and the validity of their interpretation is discussed later, in section 4.2. Briefly, aspects of network organization include: integration, how well connected each node is in the network, measured by characteristic path length and efficiency; segregation, how much the network falls into strongly interconnected subgraphs or clusters, measured by clustering coefficient (CC) and modularity; and infrastructure, characterising how certain nodes of a network tend to connect the clusters, measured by node centrality, rich club coefficient and small worldness.

CP is associated with widespread reduction in connectivity and reduced WM integrity, especially long range fibres, and those associated with the sensorimotor network. This is related to a greater characteristic path length, and a corresponding drop in global efficiency [Englander et al., 2013, Pannek et al., 2014]. Nodewise analysis also the nodal efficiency of the precentral gyrus and right middle frontal gyrus of particularly reduced [Jiang et al., 2021].

ASDs are thought to be related alterations of neural connections [Yamasaki et al., 2017]. Analysis of whole brain structural networks has shown a shorter characteristic path length, and greater local connectivity [Li et al., 2014]. A separate analysis of the rich club (RC) coefficient showed a stronger RC organisation in ASD individuals, with a greater connectedness within the RC [Ray et al., 2014].

Epilepsy is thought to be a disorder of brain network organisation.Many studies have been done to characterise the evolution of functional networks during seizures, with robust changes to CC and Characteristic path length observed [Kramer and Cash, 2012, Engel et al., 2013]. Structural network analysis is less common, and often focuses specifically on important regions or tracts. These have found widespread disconnections in the temporal lobes of those suffering from temporal lobe epilepsy. In a study of medial temporal lobe epilepsy, increased global clustering coefficient, and regional changes to node degree, efficiency, CC and betweenness centrality were found [Besson et al., 2014, Bonilha et al., 2012].

Alzheimer's Disease (AD), though not known to be related to VLBW/VP births, is a disease which has had many network based analyses. Good test re-test reproducibility for the CC, characteristic path length, degree, global efficiency, modularity, local efficiency, and betweenness centrality have been found for AD [Welton et al., 2015]. For this reason, these metrics are included in the analysis of the VLBW cohort.

1.5 Exploration of structural networks

Structural network analysis is an exciting, developing field, with techniques being continually revised, tweaked and re-written to improve the accuracy and reliability. A comprehensive evaluation of the best processing pipeline, from scanning, preprocessing, tractography, normalisation, selection and calculation of metrics, is a mammoth task far beyond the scope of this thesis. Here, techniques and measures are chosen which are well established in literature, and representative of what a 'typical' analysis might look like. While they mostly seem robust, I have been interested in, and have investigated the normalisation of the streamline count matrix, and some generalisations of binary network measures to their weighted counterparts.

A novel normalisation algorithm, node strength normalisation (NSN), was developed and used alongside the traditional waytotal normalisation to gauge its performance. Metrics are also evaluated under both normalisation schemes, and their validity is discussed.

1.6 Research aims

This thesis investigated the long term effects of being born VLBW/VP on WM integrity and organisation, through use of diffusion-weighted MRI. This project included two parts: tract-wise analysis, and whole brain structural network analysis.

Tract-wise analysis used tractography with established masks to isolate whole WM tracts in each individual. This allowed comparisons of DTI measures and volumes for each tract between adults born VLBW and age-matched controls born with normal birthweight.

Structural network analysis used tractography to find the strength of the connections between anatomically distinct regions of GM. This was used to find properties of the structural network topology thought to depict important aspects of organisation, including integration, segregation, hubs and network infrastructure.

Structural network analysis is a developing field. Through the research and implementation of network analysis, a significant amount of work went into understanding and evaluating the methods and metrics used. In addition, a novel algorithm to normalise connection matrices was developed and used alongside the traditional method, with the intention of improving the validity of results. This evaluation and innovation formed a secondary aim of this thesis.

2 Data and methods

2.1 The 1986 cohort

The 1986 New Zealand VLBW study is a nation-wide multidisciplinary investigation into child health and development. In the multiple assessment waves since it began, aspects from cardiovascular health to cognitive function have been investigated. The initial study focused on retinopathy, and enrolled all 411 infants born between 500-1499g (inclusive) in New Zealand in 1986 [Darlow, 1988]. Since then, three follow up assessments have been carried out, as summarised in table 1. At age 7-8, a health and neuodevelopmental assessment was completed [Darlow et al., 1997]. This was followed by a short followup at age 23-24 [Darlow et al., 2013], and a two day health and neuropsychological assessment, with cranial MRIs for 150 VLBW and 50 controls at 26-30 years [Darlow et al., 2015]. It is the diffusion MRI scans from the age 26-30 study which form the basis of this thesis.

A control cohort of 100 healthy, term born adults was gathered for the age 26-30 health and neuropsychological assessment. Controls were selected either by peer nomination from cohort members, or random sampling from electoral rolls. Balance for gender, ethnicity and regional distribution was maintained.

Initial funding was available for 200 cranial MRI scans. Adults born extremely preterm (EP, <28 weeks) were prioritised, as this group is known to have higher rates of neuro-developmental issues. Three of the 57 EP individuals were excluded: one with a cerebral shunt, one who was pregnant at the time of MRI assessment, and one with extreme claustrophobia. One further scan was corrupted by motion and unusable. A further 96 VLBW individuals were randomly selected for scanning, bringing the total number in this group to 150. Four VLBW scans did not include diffusion sequences, due to time constraints or claustrophobia cutting the scanning session short. A further VLBW scan was excluded due to severely disrupted anatomy. Two additional scans were carried out to supplement those excluded due to anatomical reasons. Finally, five VLBW scans were excluded from the diffusion analysis due to excess movement during this imaging sequence (see 2.4).

The first 50 term born individuals to agree to scanning formed the control group. One control scan was excluded, as it had excess movement during the diffusion sequence.

In total, the final diffusion cohort consisted of 141 VLBW and 49 control participants, as summarised in table 2.

Age, years	Included in study	Deceased	Declined	Untraced/Overseas
0.2	313	74	25	—
7-8	298	86	7	21
23-24	230	88	—	58
26-28	250	89	38	35
26-30 (MRI)	150	—	—	—

Table 1: Studies conducted with the VLBW cohort, with numbers of participants, as per [Pascoe et al., 2019, Darlow et al., 2015, Darlow et al., 1997, Darlow et al., 2013].

Ethics

The study received ethical approval from the Upper South B Regional Ethics Committee (superseded by the Southern Health and Disability Committee) (ref: URB/12/05/015).

2.2 Initial data collection

Variables of interest including birthweight, sex and gestational age were determined at birth, and were available for use in this thesis.

2.3 Scanning protocols

All scans were carried out on the same 3T General Electric HDxt scanner (GEHealthcare, Waukesha, USA) with an eight-channel head coil. The full hour-long protocol included multiple scan types: T1-weighted structural (SPGR), resting state functional MRI, arterial spin labelling perfusion MRI, T2-weighted and T2-weighted FLAIR images, and DTI. The DTI acquisition analysed here was as follows:

> A 2D diffusion-weighted, spin echo, echo planar imaging sequence was used to measure microstructural integrity, with diffusion weighting in 64 uniformly distributed directions (b = 1000 s/mm^2) and 8 acquisitions without diffusion weighting (b = 0 s/mm^2): TE/TR = 96/10000 ms, flip angle = 90 deg., acquisition matrix = 128 × 128 × 74, FOV = 250 mm, slice thickness = 2 mm, voxel size = 1.95 × 1.95 × 2 mm^3, NEX = 1, ungated [Pascoe et al., 2019].

Data acquisition for this study began prior to the routine acquisition of reversed phase encoding images that allow the correction of susceptibility distortions in diffusion-weighted data. As these were not acquired, full susceptibility distortion correction using FSL's TOPUP could not be done.

Group	Scans performed	Scans excluded: Movement	Incomplete/missing	Disrupted anatomy	Scans used
VLBW	152	5	4	2	141
Controls	50	1			49

Table 2: Scans carried out, and reasons for rejection.

2.4 Data pre-processing

A limited number of pre-processing steps had already been performed on this dataset. To allow for tractography to be performed, I have extended this process, and re-run steps which were incomplete on some subjects.

Image processing was carried out using FSL (v5.0.9, [FSL,]) and included the following processes:

EDDY

Movement and distortion and correction was carried out using EDDY [Andersson and Sotiropoulos, 2016]. Our diffusion imaging sequence comprised of 72 images across 12 minutes. The extended duration of this sequence allows ample time for patient movement, which needs to be estimated and corrected. The threshold for exclusion due to movement was set at greater than 2 voxels (4mm) for absolute motion (relative to first acquisition), or greater than 3σ for relative motion (relative to the previous acquisition). Five VLBW scans and one control scan were rejected due to excessive movement, as per section 2.1. The large, rapidly changing gradients used in DWI induce eddy currents which in turn cause image distortions. It is crucial to correct for these and ensure proper registration, with each voxel in each image depicting the same volume within the brain, so diffusion can be correctly characterised.

DTIFIT

Fitting of a diffusion tensor model (as per section 1.2) was done using DTIFIT. These are fit under a bayesian framework, with uninformative priors, beyond keeping values positive where appropriate [Behrens et al., 2003]. Along with the diffusion tensors, voxelwise measures including FA, MD, AD and RD were calculated, as per section 1.2.

BEDPOSTX

BEDPOSTX fits the ball-and-stick model of fibre populations in each voxel which is used by the tractography algorithm. This model comprises of an isotropic component, representing noise and scattered fibres, and one or more infinitely anisotropic components, representing the main fibre population(s). Automatic relavence determination is used to find the number of fibre populations evident in each voxel. This model is then used by the tractography algorithm for streamline tracing [Behrens et al., 2007, Jbabdi et al., 2012, Behrens et al., 2003].

Some subjects had incomplete/missing BEDPOSTX results, which were re-run and completed successfully.

FNIRT and inverse FNIRT

A mapping between each subjects' FA image and the standardised Montreal Neurological Institute (MNI) space was found using FNIRT, and inverse FNIRT to find the reverse transform. This allows the masks for XTRACT and parcellation for network analysis, both of which are specified in MNI space, to be transformed into subject space. FNIRT works by first applying a linear warp (affine transformation) then iteratively building a local, non-linear deformation field of increasing resolution [Andersson et al., 2007b]. This allows for regional variations, such as enlarged ventricles, to be accounted for, ensuring good registration of the masks and nodes.

2.5 Tractography

Subsequent to this pre-processing, tractography was run in two ways: to identify and extract DTI metrics from WM tracts of interest, and to form structural connectivity graphs.

Tractography is in principal a simple process, following a basic loop:

1. Seed a streamline. The default of 5000 streamlines per voxel in the seed mask was used.

2. Draw a sample orientation from the orientation density function (found by BedpostX) of nearby voxels.
3. Take a step in that direction. The default step size of 0.5mm was used
4. Check if a termination criterion was met:
    - Termination mask
    - Maximum length
    - Too steep a turn, default of $\approx 80^o$ was used
5. Stop if termination criteria is met, or repeat from 2.

This results in a path through the brain, following the direction of the WM.

2.6 Tract identification with XTRACT

I have used XTRACT to identify the 42 well defined tracts shown in table 3. XTRACT runs with known, prespecified masks, which are transformed into subject space for tractography. Seed and target masks are placed at either end of a WM bundle, and exclusion masks are placed to remove streamlines which stray onto other tracts [Warrington et al., 2020]. Each streamline adds to a heatmap, which is thresholded to create a mask isolating each WM tract in each subject's diffusion space. These WM masks are then used to extract key metrics including volume and mean, median and variance for each of FA, MD, RD, AD and length. An example of this process can be seen in figure 3.

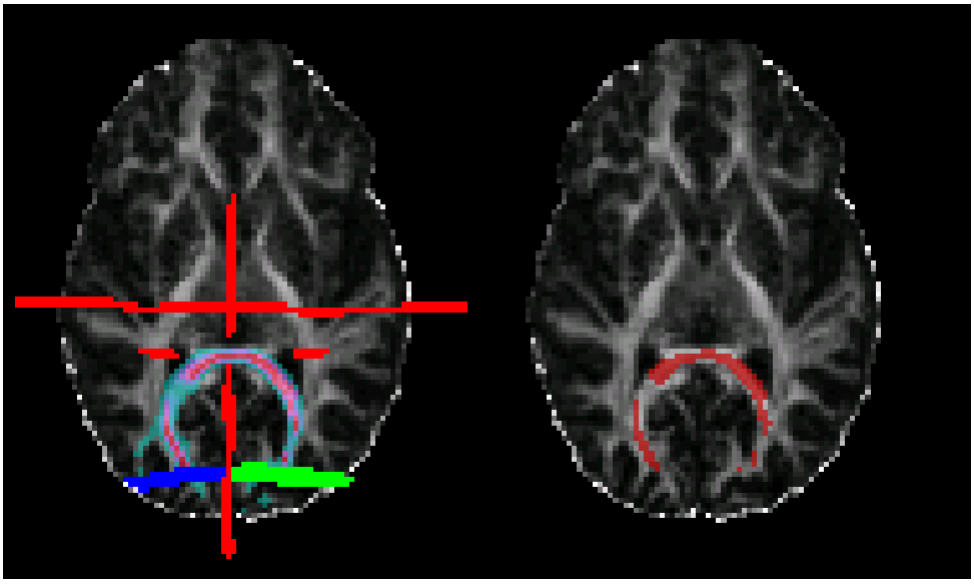

Figure 3: FSLs Xtract masks for isolating the forceps major. Left: seed (green) target (blue) and exclusion (red) masks, with tract heatmap in cyan/pink. Right: example thresholded heatmap, to isolate voxels along the forceps major.

Tract	Abbreviation
Arcuate Fasciculus	AF
Acoustic Radiation	AR
Anterior Thalamic Radiation	ATR
Cingulum subsection : Dorsal	CBD
Cingulum subsection : Peri-genual	CBP
Cingulum subsection : Temporal	CBT
Corticospinal Tract	CST
Frontal Aslant	FA
Forceps Major	FMA
Forceps Minor	FMI
Fornix	FX
Inferior Longitudinal Fasciculus	ILF
Inferior Fronto-Occipital Fasciculus	IFO
Middle Cerebellar Peduncle	MCP
Middle Longitudinal Fasciculus	MdLF
Optic Radiation	OR
Superior Thalamic Radiation	STR
Superior Longitudinal Fasciculus 1	SLF1
Superior Longitudinal Fasciculus 2	SLF2
Superior Longitudinal Fasciculus 3	SLF3
Anterior Commissure	AC
Uncinate Fasciculus	UF
Vertical Occipital Fasciculus	VOF

Table 3: Tracts found by Xtract, as per [Warrington et al., 2020]

2.7 Network construction

I have also constructed structural connectivity matrices for graph theoretical analysis. The parcellation used was Automatic anatomical labelling atlas 3 (AAL3), and streamlining was run between each region as per 2.5. These matrices were normalised both by waytotal and node strength normalisation, and subsequently used to calculate the graph metrics analysed below.

2.7.1 Parcellation

Automatic anatomical labelling atlas 3 (AAL3; [Rolls et al., 2020]) at 2mm resolution was used for this analysis. This was decided due to AAL's common, long-standing use in literature, having been used for both structural and functional analyses of various conditions and disorders [Tzourio-Mazoyer et al., 2002, He et al., 2018, Disselhoff et al., 2020, Qi et al., 2015]. The AAL atlases are based on a single-subject high resolution T1 image formed from 27 acquisitions from the Montreal Neurological Institute in 1998 [Tzourio-Mazoyer et al., 2002]. This image was divided into the current 166 ROIs based on anatomical features via automatic sulci detection and manual segmentation.

AAL3 is offered in both 2mm and 1mm resolution. The 2mm resolution was used to match the resolution of the diffusion images, and to lower computation time.

FSL's ProbtrackX allows for ROIs to be specified in either subject (diffusion) space or in any other space, as long as transformations to and from said space are provided. Both diffusion and MNI spaces were trialed. ROIs were eroded when writing parcellations to diffusion-space, as shown in figure 4. Due to this, AAL3 was provided to ProbtrackX in MNI space, along with forward and inverse warps to each subject's diffusion space.

To confirm the appropriateness of the warping method, linear and non-linear warps, produced using FSL's FLIRT and FNIRT [Jenkinson and Smith, 2001, Jenkinson et al., 2002, Andersson et al., 2007a], were visually compared as per figure: 4. The non-linear warp was chosen due to overall better conformance to the frontal lobes and internal structures such as the thalamus. This is especially important here, as DWI is commonly associated with susceptibility artefacts. These cause an elongation of the frontal lobes, and to a lesser extent an indentation of posterior regions (this direction depends on the direction of phase encoding, for this dataset it ran anterior-posterior). This deformation is partially corrected for in FSL's EDDY, but the linear warps still tended to undershoot the frontal regions. The non-linear warps generally seem to overshoot the external bounds of the brain, however this is not of concern, as a brain mask is applied at the time of tractography, nullifying any streamlines beyond the cortex.

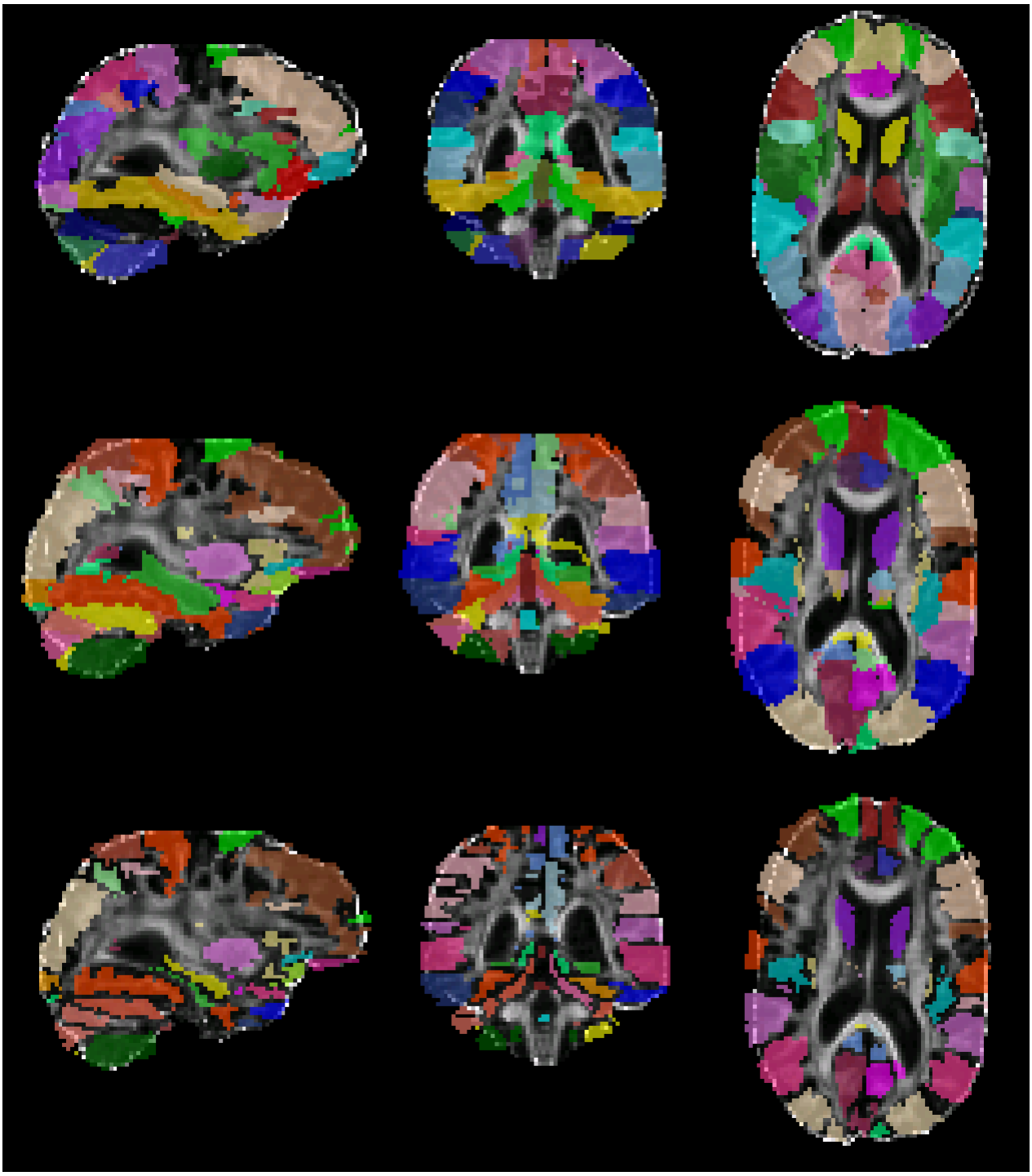

Figure 4: Automated anatomical labelling atlas 3 parcellation (colour) in subject space via linear (top) and non-linear (mid, whole mask transform, and bottom, ROIs transformed individually) transformations. These are overlaid on a subject's fractional anisotropy image (greyscale). Views (left to right) are Sagittal, axial, and coronal. Views are in radiological convention (left is right).

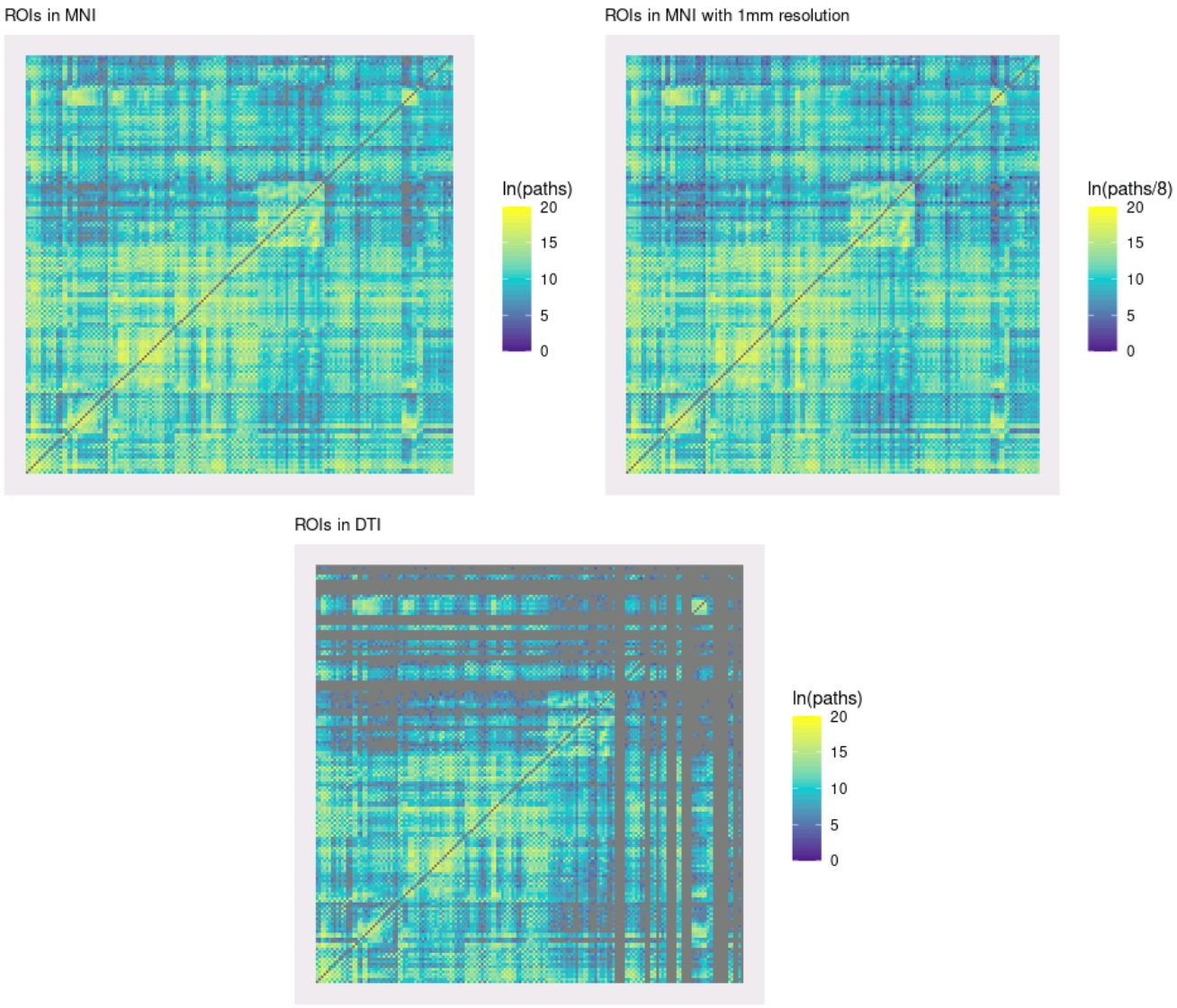

Figure 5: Connection matrices of a single subject, produced with a variety of settings. Top-left shows the settings which were used applied to the whole dataset: AAL3 in 2mm resolution in MNI space, related to subject space using a non-linear warp. This is very similar to the top-right matrix, which used AAL in 1mm resolution. About 50 of the 27000 connections were found to deviate by more than an order of magnitude. Bottom shows the tractography done in DTI-space: noteably many ROIs have no connections, as those regions were completely eroded by the transformation.

2.7.2 Normalisation

The output of ProbtrackX's network tractography is an observed matrix, O_{ij}, where each element is the observed number of streamlines (NoS) from ROI i to ROI j. As the NoS efferent from an ROI is proportional to the size of that ROI, normalisation must be done to prevent large ROIs from artificially appearing more connected due to their size. Furthermore, the constant

of proportionality is a parameter of the ProbtrackX program, so normalisation is neccesary to compare studies.

A common normalisation technique is by waytotal: dividing each observed NoS by the total NoS originating in that ROI. This makes the strength of each edge be interpretable as the proportion of connectivity from each region. This however introduces a bias against well connected regions, as can be seen in the following example.

Consider running probabilistic tractography on the undirected graph depicted in figure 6 (top), with two edges of weights one and three. The streamlining process is the culmination of dozens of random steps, ultimately leading each streamline to one of the other ROIs, or to terminate without being counted. This may be modelled as each streamline 'choosing' a destination ROI probabilistically, weighted by the strength of the corresponding edges. Applying this to the example graph, we would expect 100% of (counted) streamlines from nodes A and C to reach node B, but from node B, for 1/4 to travel to A, and 3/4 to C, as shown in the directed graph in figure 6 (bottom). This is equivalent to normalisation by waytotal, and is clearly non-representative of the underlying connectivity.

With the knowledge that the underlying true graph should be symmetric, due to the symmetry of DWI, we can leverage the asymmetries in O to reconstruct the true connection matrix T, up to a constant.

To find T, consider the formation of the observed connection matrix O. An observed edge O_{ij} will be the product of the number of streamlines seeded at that node (waytotal), $\sum_a O_{ia}$ and the proportion of true node strength (sum of edge weights leaving node i), $\sum_a T_{ia}$, belonging to edge T_{ij}. This gives the equation and rearrangement

$$O_{ij} = \frac{T_{ij}}{\sum_a T_{ia}} \sum_a O_{ia} \tag{3}$$

$$T_{ij} = \frac{O_{ij}}{\sum_a O_{ia}} \sum_a T_{ia} \tag{4}$$

For simplicity of notation, let O be normalised by waytotal, $\sum_a O_{ia} = 1$, and let the row weights of T be denoted $t_i = \sum_a T_{ia}$. Equation 4 becomes

$$T_{ij} = O_{ij} t_i \tag{5}$$

If we assume that, since diffusion data cannot reveal the direction of a WM pathway, the theoretical matrix is symmetric,

$$T_{ij} = T_{ji} \tag{6}$$

We may substitute the above two equations.

$$O_{ij} t_i = T_{ij} = T_{ji} = O_{ji} t_j \tag{7}$$

This gives us an equation relating each pair of row (or column) sums in T:

$$O_{ij} t_i - O_{ji} t_j = 0 \tag{8}$$

for $\{i,j \in 1,2,3...n \mid i < j\}$. This may be gathered into a, overspecified matrix equation

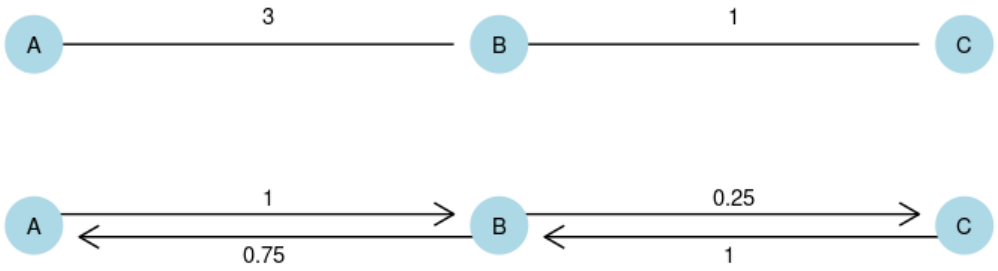

Figure 6: Example true graph (T, top), and the graph observed from random streamlining on T, and normalising by waytotal (O, bottom)

$$A\vec{t} = \vec{0} \tag{9}$$

In the ideal case, where O is free of noise, this may be solved directly by finding the nullspace of A. If noise is present, the nullspace of A is trivial ($\vec{t} = \vec{0}$). In this case we can estimate $\vec{t}$ based on the mean squared error (MSE), given by

$$MSE = t^T A^T A t \tag{10}$$

This will also be minimised by the trivial solution $\vec{t} = \vec{0}$; indeed, even if the true value of t were known, MSE would grow as T is scaled. It should be noted that only information on the ratios between elements of $\vec{t}$ is known, so T can only be reconstructed to an arbitrary scaling.

To find a useful solution, a t which minimises the mean squared error for a given matrix weighting ($\|t\|$) is found (equivalently t which minimises growth of MSE with scaling of t). This will be the eigenvector with the least eigenvalue of $A^T A$. It is perhaps simplest to justify this by considering eq. 10 as specifying an ellipsoid (in t space) for a given MSE. The major axis, which is given by the eigenvector with the least eigenvalue, will always give the point(s) furthest from the origin with a given MSE. This solution is equivalent to solving the least squares problem with $\|t\| = 1$, and is sensible as the scaling of $\|t\|$ (and by extension the reconstructed T) is arbitrary.

This novel approach, which I refer to as Node Strength Normalisation (NSN), to connection matrix normalisation provides an estimate of the true connection matrix, who's elements are interpretable as the strength of the connection between ROIs, relative to each other of that subject's connections. NSN boosts the connections of well connected nodes, and diminishes those of less, by allowing the total strength efferent from an ROI to vary above or below 1. It also provides two estimates for each edge, as T is assumed to be symmetric. In this analysis, the average of these is used.

NSN was implemented in MATLAB, and that code is available at www.github.com/LiamBignell/NodeStrengthNormalisation.

NSN does not account for the lower weights we would expect to see for long range connections. This is a known issue with tractography, with current solutions being a tradeoff between specificity and sensitivity. As such, no distance corrections are used in this analysis.

Brain property	Graph measure	
Segregation	Global Clustering Coefficient	C
	Local Clustering Coefficient	C_i
	Modularity	Q
Integration	Characteristic path length	L
	Global efficiency	E
Hubs and	Betweenness centrality	$g(v)$
infrastructure	Rich club coefficient	$\phi(r)$

Table 4: Graph metrics included in analysis, with symbols.

This thesis examines structural connectivity networks using both standard waytotal normalization, as well as my proposed Node Strength Normalisation (NSN).

2.7.3 Thresholding

Initial work on graph theoretical networks focused on binary networks, those where edges were either present or absent, with no indication of their strength. To achieve these, thresholding of the connection matrices is done, removing the weakest edges, and setting remaining edge weights to one. This discards a large portion of the information present, and so generalisation of network metrics to weighted graphs have been proposed, and commonly adopted. With these, the information present in the edge weights may be retained.

This analysis was done with no thresholding. Scrutiny of the graph metrics used here found some metrics behaved poorly on totally un-thresholded graphs. Some thresholding was trialled, but due to multiple comparisons issues, could not be included in the statistical analysis. This is discussed further in section 4.2.

2.7.4 Graph properties

One difficulty in network analysis is selecting significant and interpretable properties to investigate. For this analysis, seven metrics were selected, as summarised in table 4. In selecting these, consideration was given to representation in literature, interpretability, representation of various topological properties, and reproducibility. Many of these metrics were popularised in [Rubinov and Sporns, 2010], which both highlights some topological properties observed in the human brain, and how they are demonstrated by a variety of metrics. This paper also introduces software to calculate them (Brain Connectivity Toolbox; BCT). This is the toolbox used to calculate all metrics except rich club. Specific algorithms are discussed in section 4.2.2.

These metrics can broadly be categorised by the underlying properties they are reported to represent, as follows:

Integration

Perhaps the most understandable of the network topology ideas is that of integration. Strongly integrated networks are ones in which any two nodes are 'near' each other, either having few and/or strong edges along path(s) between them.

Characteristic path length, L is calculated as the mean shortest path between each pair of nodes. For weighted graphs, the 'length' of an edge is taken as the inverse of its strength.

Efficiency, E, is calculated as the mean of the inverses of the shortest path length between each pair of nodes. This makes E closely related to C, but where C is more heavily influenced by longer paths, E is more influenced by the shorter paths. This is particularly important if any nodes become disconnected; if no paths between two nodes exists, C will become infinite, whereas E will remain bounded.

Segregation

Topological segregation is based on the idea of groups of nodes strongly integrating amongst themselves, but weakly to nodes in other groups. Scale becomes an important factor here, as groups may in turn be comprised of sub-groups. The formation of the nodes themselves hints at a finer community structure, where voxels are grouped together by their propensity to work together as a group. This structure continues down to the scale of cortical columns/mini-columns, formed from individual neurons, as discussed in 1.4. As such, these measures identify only macro-scale clusters, appropriate to the size of the regions.

Clustering coefficient (CC) is a common measure used to quantify clustering in a network. A node's CC is the proportion of pairs of nodes, which both connect to the first, which connect also to each other. CC is defined on each node separately, and the mean of these gives the global CC. A proper explanation and evaluation of the generalisations of these to the weighted case is given in section 4.2.2.

Modularity, Q, is the other value used here to quantify segregation. Modularity evaluates the quality of a particular grouping of nodes by calculating the fraction of edges falling within the given groups, minus the expected fraction for an equivalent random network. The idea of an 'equivalent random network' is quite involved; to skirt around this topic, the average of graphs with the same degree distribution is used. This is known as the configuration model [Newman and Girvan, 2004]. Modularity captures the idea that a good clustering should have much greater connectivity within the group than we would expect by chance. This ranges from -0.5 indicating only without group edges to 1, indicating only within group edges. Modularity requires a pre-specified grouping, which has been done here using the Louvain method [Blondel et al., 2008].

Hubs and infrastructure

Small-world networks are those which display both higher segregation (clustering) and better integration (lower path lengths) than random graphs. Both aspects of small-world networks are assumed to be necessary for optimal information processing [Sporns, 2011, Stam, 2010]. These networks are commonly characterised by smaller, relatively isolated communities with strongly interconnected hub nodes.

The hub nodes sit on the boundary of communities, and allow for both high segregation and integration. Identifying and quantifying these hub nodes may be done in several ways. Most simply is node degree - the number of edges connecting to a node, or for weighted networks, strength - the sum of the connecting weights. This is sometimes referred to as the degree centrality. This shows how connected a node is locally, but may not capture its placement within the wider network. To capture wider dynamics, betweenness centrality may be used.

Betweenness centrality counts the number of shortest paths each node is involved in. Those

nodes which are highly central will be involved in many paths, and thus have a high betweenness centrality. Nodes with a high Betweenness centrality were thought to be highly influential in the control of information flow, or key in coordinating the network [Freeman, 1977]. These highly central nodes are also of interest in the context of network resilience. Disruption to those hubs poses a greater risk in networks with fewer hub nodes [van den Heuvel and Sporns, 2013].

Rich club, $\phi(r)$, is the final metric included here, and aims to describe how strongly connected the 'richest' nodes are. The rich club is thought to be comprised of the hub nodes, and forms when the richest nodes preferentially connect with each other (more than would be expected by chance). This organisation is thought to enable efficient communication [Kanel et al., 2021]. Nodes and edges are ranked based on a 'richness' measure, r. For a given richness, the total strength in the subgraph containing only those nodes richer than r, denoted $W_{>r}$ is compared to the total strength among the E strongest edges in the full graph, where E is the number of edges present in $W_{>r}$. By varying r, a rich club curve can be plotted as the exclusiveness of this club is varied [Opsahl et al., 2008b].

The implementation used in BCT used node degree as the richness parameter, r. This was found to behave particularly poorly when thresholding was not applied. Instead, node strength was used. This eliminates the possibility of using waytotal normalisation (as node strengths are all set to 1), so only normalisation with NSN is reported. This is further discussed in section 4.2.2. r was varied from 0 (all nodes) to 500 (5% of nodes).

2.8 Statistical analysis

Linear regression was used to perform groupwise comparisons between VLBWs and controls. Age and sex were included as covariates, as these are known to have an effect on brain structure; all statistics shown have been adjusted for age and sex. When running multiple models across a number of WM tracts and network nodes, false discovery rate (FDR) was controlled using the BenjaminiHochberg procedure. The corrected p-values are displayed as 'q-values', and are considered significant at $q<0.05$.

ROI metrics

Two approaches were used to analyse tract-wise data. Firstly, a direct comparison as per above, with an independent comparison between VLBW and control for each tract (with FDR correction). Secondly, principal component analysis (PCA) was used to analyse data-driven groups of tracts. In this instance, PCA was used both as a data-reduction procedure, and to highlight tracts with a high covariance. In this manner, we expect tracts involved in the same network to appear in the same principal component (PC). The top five PCs were retained for further analysis. The contributing tracts from those with a significant group difference are reported.

Xtract's reconstruction finished unsuccessfully in 61 of the 7980 reconstructions. These were spread across 47 subjects, and 9 tracts. Most notable is the Fornix, both left and right, which had 16 subjects with no volume. Missing values were excluded from linear regression, and imputed for PCA. Data imputation was carried out using multivariate imputation by chained equations [Buuren and Groothuis-Oudshoorn, 2011].

Network metrics

As with WM tracts, graph theoretic metrics were analysed using linear regression to find groupwise differences. Where metrics are found on a node-wise basis, independent FDR corrections were done. Rich club coefficient naturally has a significant degree of correlation between similar r values. As such, BenjaminiHochberg FDR correction was not appropriate. Due to time constraints, FDR was not controlled for.

Software

Statistical analysis was carried out with R in RStudio [R Core Team, 2022, RStudio Team, 2022]. Important packages included mice (interpolation) [Buuren and Groothuis-Oudshoorn, 2011]; ggplot2 (ploting) [Wickham, 2016]; factoextra (PCA) [Kassambara and Mundt, 2020]; tidyr and dplyr (data manipulation) [Wickham and Girlich, 2022, Wickham et al., 2022]; tidygraph (creating graphs in R) [Pedersen, 2020]; and ggraph (graph visualisation) [Pedersen, 2021]

3 Results

3.1 White matter tract comparisons

The results from the direct comparisons of WM pathways found several tracts with lower volumes in the VLBW group, largely with similar FA and MD (as per figures 7 to 9, and tables 11 to 13). Tracts with reduced volumes bi-laterally included the acoustic radiations, inferior longitudinal fasciculus, and superior longitudinal fasciculus III; in addition to the left peri-genual cingulum subsection, cortico-spinal tract and superior thalamic radiation; the right fornix; and the forceps major and minor. For DTI measures, only three tracts survived FDR correction. The left temporal cingulum subsection (hippocampal white matter) and the forceps major exhibited both reduced FA and increased MD in the VLBW group relative to controls; the right optic radiation also showed significantly higher MD in VLBW compared to controls.

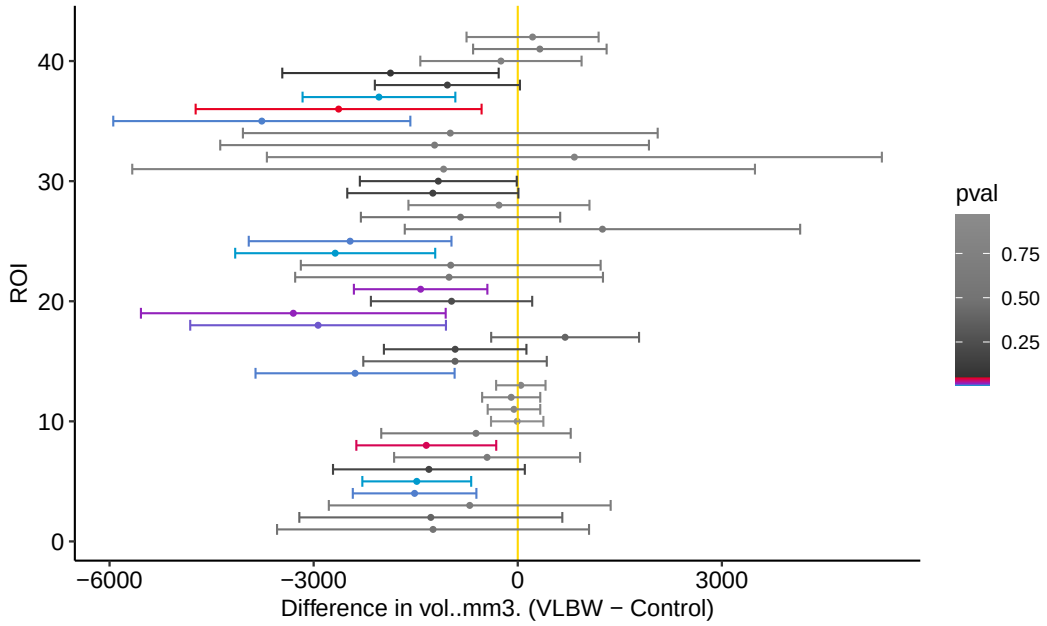

Figure 7: 95% confidence intervals for each tract's mean difference in volume (mm^3), VLBW-Control, corrected for intracranial volume, age and sex. Numbering is per table 11. Intervals are coloured by their FDR corrected q-values, red: q = 0.05, purple: q = 0.01, blue: q = 0.001.

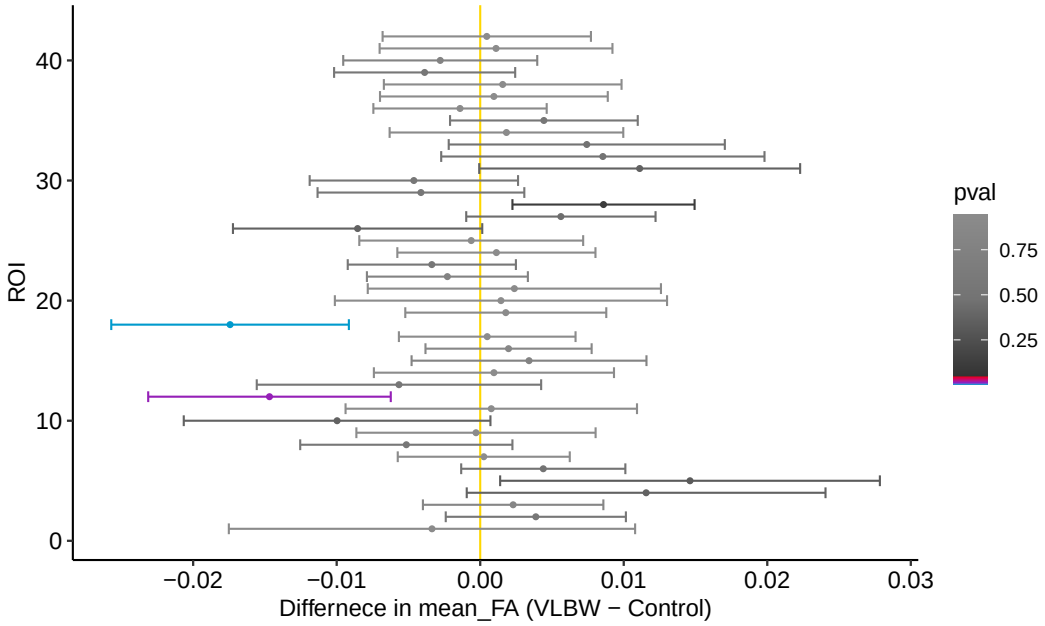

Figure 8: 95% confidence intervals for each tract's mean difference in FA, VLBW-Control, corrected for age and sex. Numbering is per table 12. Intervals are coloured by their FDR corrected q-values, red: q = 0.05, purple: q = 0.01, blue: q = 0.001.

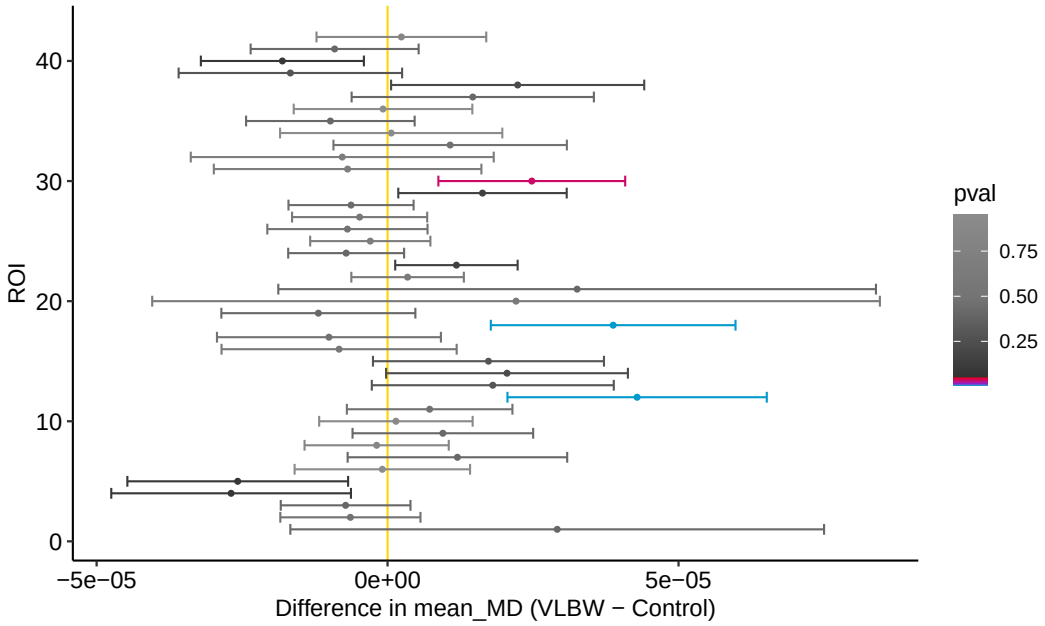

Figure 9: 95% confidence intervals for each tract's mean difference in MD, VLBW-Control, corrected for age and sex. Numbering is per table 13. Intervals are coloured by their FDR corrected q-values, red: q = 0.05, purple: q = 0.01, blue: q = 0.001.

PCA

For both FA and MD, the first five principal components were retained for further investigation. Components are shown graphically in figures 10 to 13, and numerically in tables 5, 6, 8 and 9.

For FA, the first five components explained 60.3% of the variance. Of these, the second component, which explained 8.1% of the variance, was the only to show a significant group difference ($p = 0.029$), after adjusting for age and sex (figures 10 and 11a). Primary contributors to this PC are shown in table 8.

PC	% Contribution	$\mu_{VLBW-Control}$ (σ)	t-stat	p-value
1	38.6	0.121 (0.668)	0.181	0.856
2	8.1	-0.822 (0.315)	-2.608	**0.010**
3	6.5	-0.219 (0.275)	-0.800	0.425
4	4.0	-0.155 (0.226)	-0.683	0.495
5	3.1	0.335 (0.201)	1.666	*0.097*

Table 5: The first five principal components of FA, their contribution and statistical comparisons.

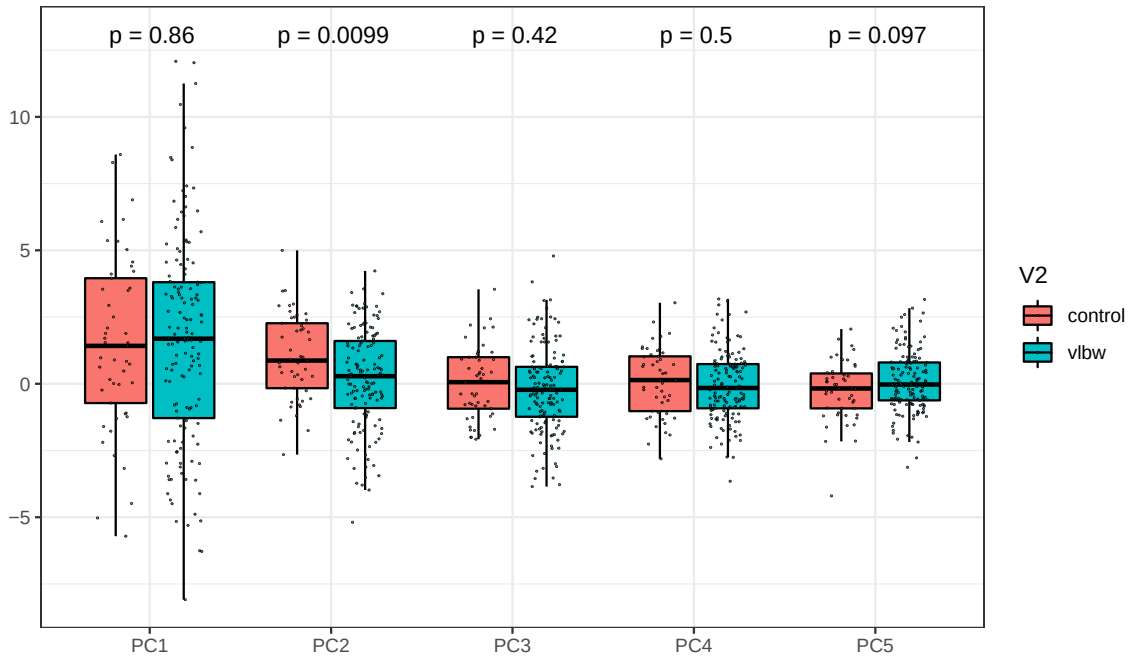

Figure 10: Group comparisons of the top five FA principal components, corrected for age at scan and sex

For MD, the first five components explained 62.2% of the variance. Of these, the fourth and fifth components were significantly different between the VLBW and control group, with p-values of >0.001 and 0.003 respectively (figure 12). Their percentage contribution of explained variance were 4% and 3.1% (figure 13a), and their major constituents are shown in table 9.

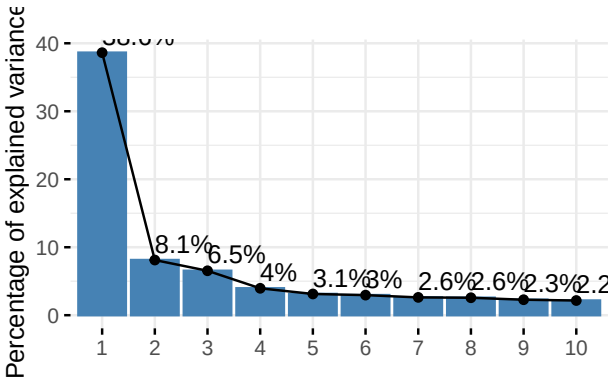

(a) Scree plot showing principal components' contribution to variance observed in the FA along tracts identified with Xtract.

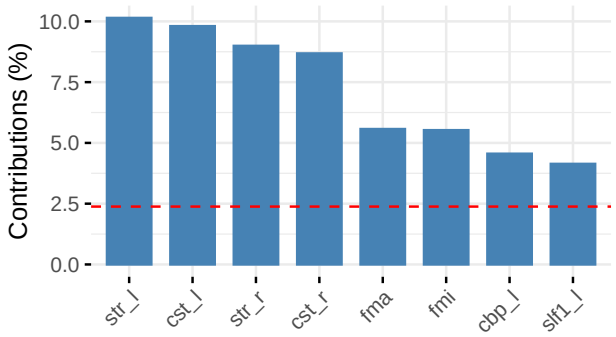

(b) Tracts contributing to the second FA-based principal component

Figure 11: FA PCA plots: scree plot and second PC.

PC	% Contribution	$\mu_{VLBW-Control^{\dagger}}$ ($\sigma^{\dagger}$)	t-stat	p-value
1	35.80	0.168 (0.687)	0.244	0.807
2	9.40	0.626 (0.343)	1.822	*0.070*
3	8.00	0.082 (0.323)	0.254	0.799
4	5.20	1.345 (0.238)	5.640	**0.000**
5	3.80	-0.642 (0.216)	-2.968	**0.003**

Table 6: The first five principal components of MD, their contribution and statistical comparisons.

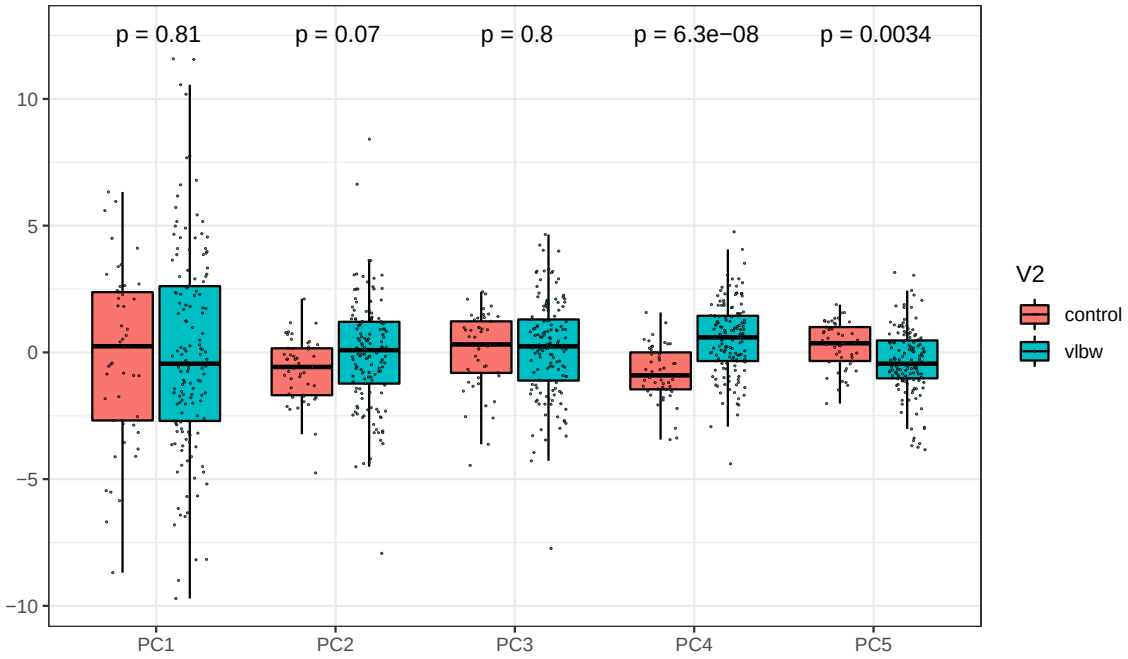

Figure 12: Group comparisons of the top five MD principal components, corrected for age at scan and sex

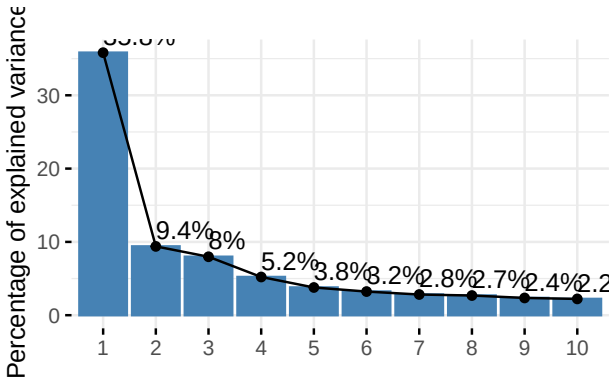

(a) Scree plot showing principal components' contribution to variance observed in the MD along tracts identified with Xtract.

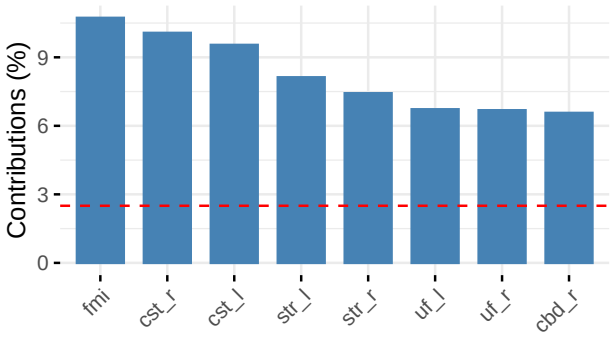

(b) Tracts contributing to the third MD-based principal component

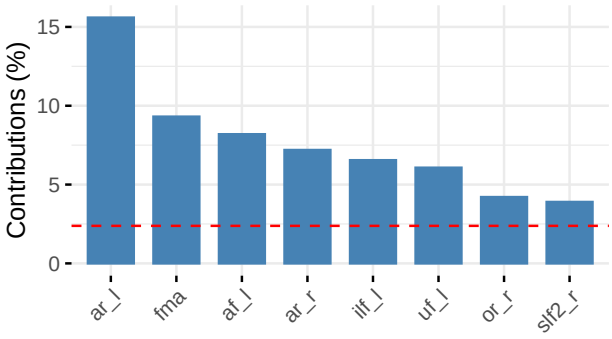

(c) Tracts contributing to the fourth MD-based principal component

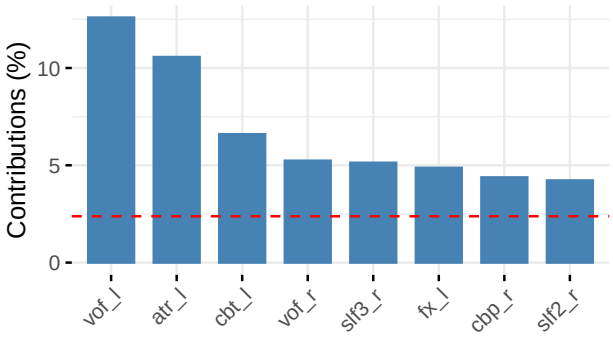

(d) Tracts contributing to the fifth MD-based principal component

Figure 13: MD PCA plots, scree plot and third through fifth PCs.

3.2 Network analysis

Global metrics

Results from the global metrics were generally consistent across both normalisation schemes, and are summarised in figure 14 and table 10. The VLBW group shows some evidence of greater integration, with a non-significantly lower characteristic path length, and greater global efficiency, significant under node strength normalisation (NSN; $p < 0.001$). Segregation measures were both significant, with the VLBW group having a greater modularity ($p = 0.02$, waytotal normalisation (Wt); $p = 0.021$, NSN), and a lower mean CC ($p = 0.015$, Wt; $p = 0.006$, NSN). The segregation results appear inconsistent, as it is generally expected that mean clustering and modularity should be positively correlated.

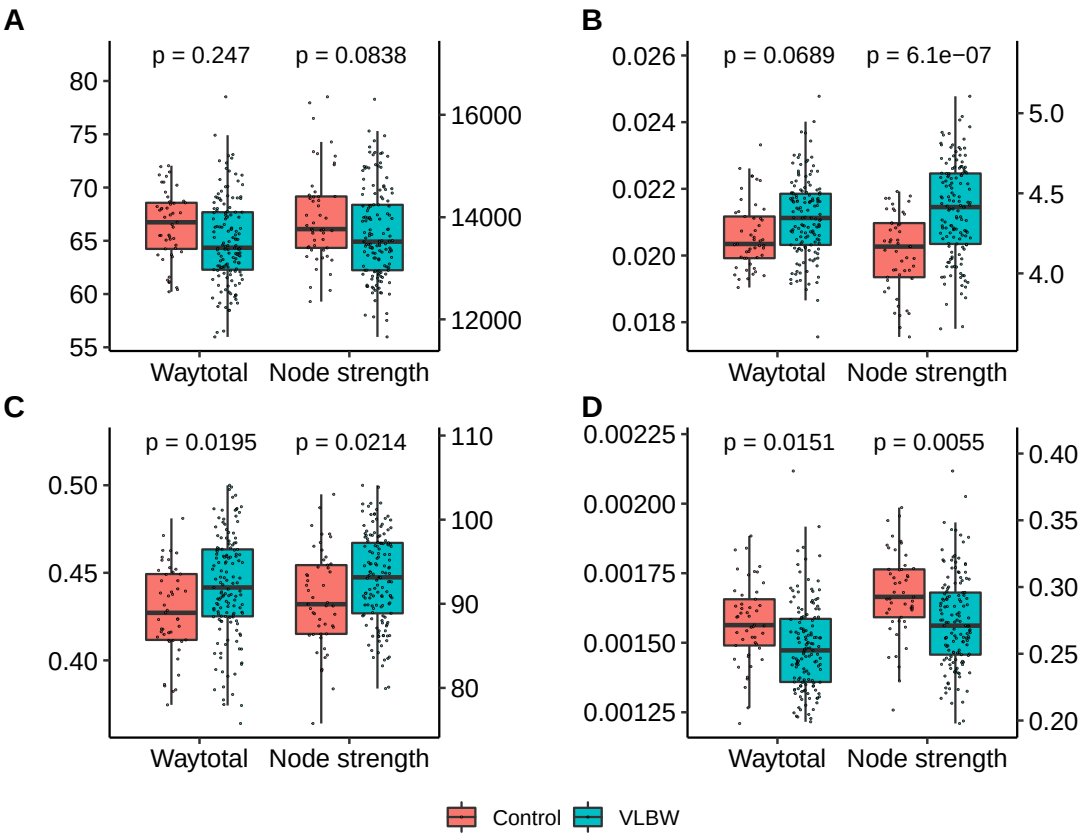

Figure 14: Single graph measures under both normalisation schemes. Group comparison p-values corrected for age at scan and sex are shown above boxplots. A and B: integration measures, characteristic path length and efficiency respectively. C and D: segregation measures, modularity and mean CC respectively.

Betweenness centrality

The differences in betweenness centrality (by node) did not reach statistical significance for most nodes, as seen in figure 16. Those which were significant, after age, sex and FDR correction, are listed in table 7.

Notably, superior frontal gyri appeared bi-laterally, with both left and right showing a significantly greater centrality under both normalisation schemes. The waytotal normalisation grouped by lobe hints that central regions may have an overall lower centrality, but this is not evident under NSN.

ROI number	ROI	μ_{diff} (Wt)	μ_{diff} (NSN)	q-val (Wt)	q-val (NSN)
1	Precentral_L	-270	2.5	0.012	0.0004
3	Frontal_Sup_2_L	700	1960	0.0015	0.0026
4	Frontal_Sup_2_R	600	1670	0.0051	0.047
9	Frontal_Inf_Tri_L	-240	-270	0.012	0.72
34	Insula_R	130	120	0.013	0.35
59	Postcentral_L	-240	-27	0.012	0.75
63	Parietal_Inf_L	-81	-29	0.013	0.26
76	Putamen_R	330	1200	0.038	0.064
151	ACC_sup_L	-45	-22	0.31	0.0004

Table 7: Nodes with a significant difference in betweenness centrality, corrected for age, sex and FDR. Difference is VLBW - control.

Node-wise clustering coefficient

The differences in CC by node, seen in figure 16, generally reflected the globally lower CC seen in VLBWs. This was particularly prominent in the central and parietal lobes. Interestingly, this trend was reversed in the cerebellum, which instead showed a slightly higher clustering in the VLBW group.

Rich club curve

The rich club curves are shown in figure 15. The VLBW group had a significantly lower RC coefficient in the cutoff range from 127 to 247 ($p < 0.05$; age and sex, but NOT FDR corrected). In this range, the RC coefficient is 0.728 to 0.567 for controls, and 0.718 to 0.556 for VLBWs.

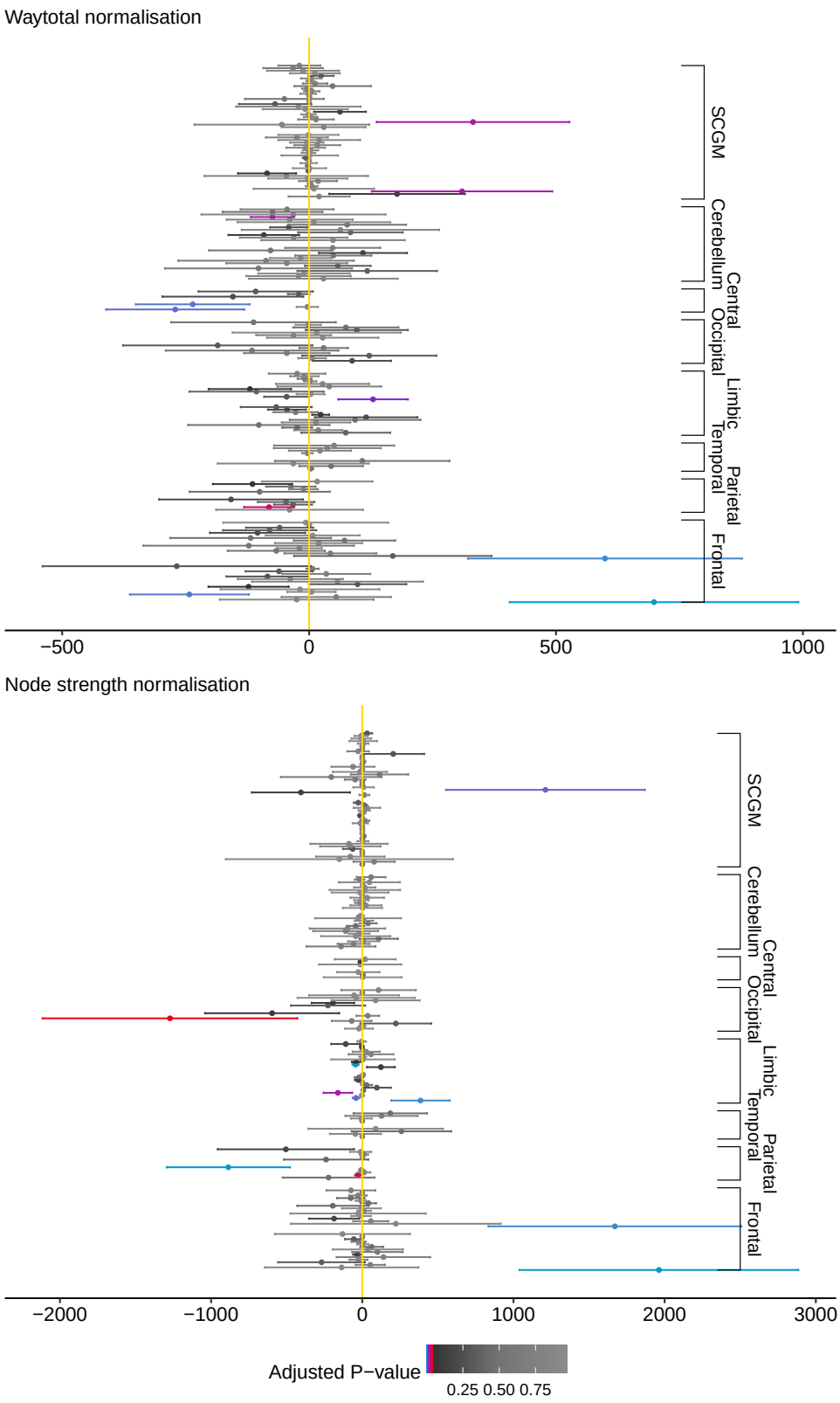

Figure 16: Forest plots for the nodewise difference (VLBW - Control) in betweenness centrality under both normalisations. The 95% confidence interval is shown before performing FDR correction, and coloured by corrected q-value (red: $q = 0.05$, purple: $q = 0.01$, blue: $q = 0.001$). Nodes are divided by lobe, and into left/right (bottom/top) hemispheres within lobe where appropriate. SCGM is sub cortical grey matter.

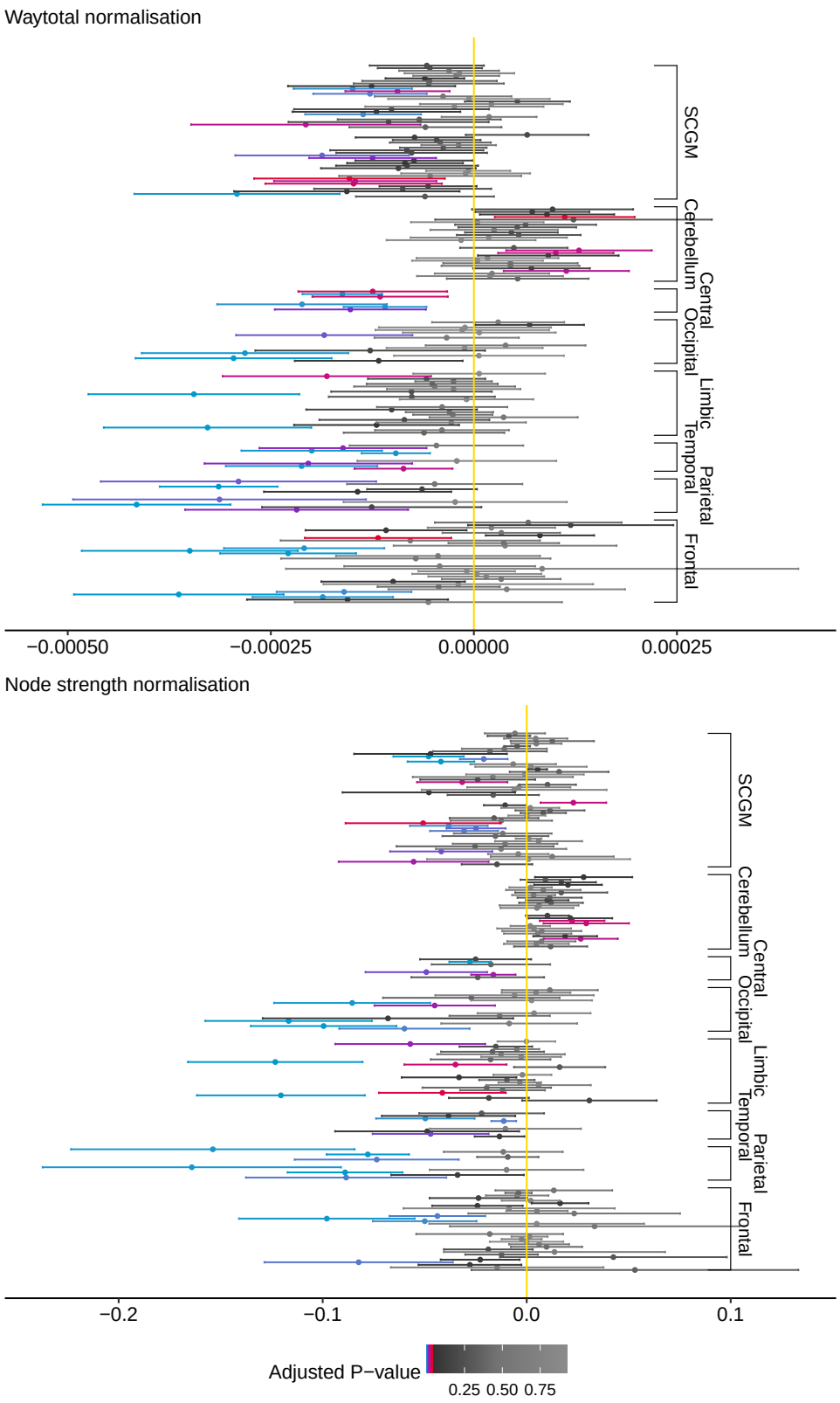

Figure 17: Forest plots for the nodewise difference (VLBW - Control) in Clustering Coefficient under both normalisations. The 95% confidence interval is shown before performing FDR correction, and coloured by corrected 1-value (red: q = 0.05, purple: q = 0.01, blue: q = 0.001). Nodes are divided by lobe, and into left/right (bottom/top) hemispheres within lobe where appropriate. SCGM is sub cortical grey matter.

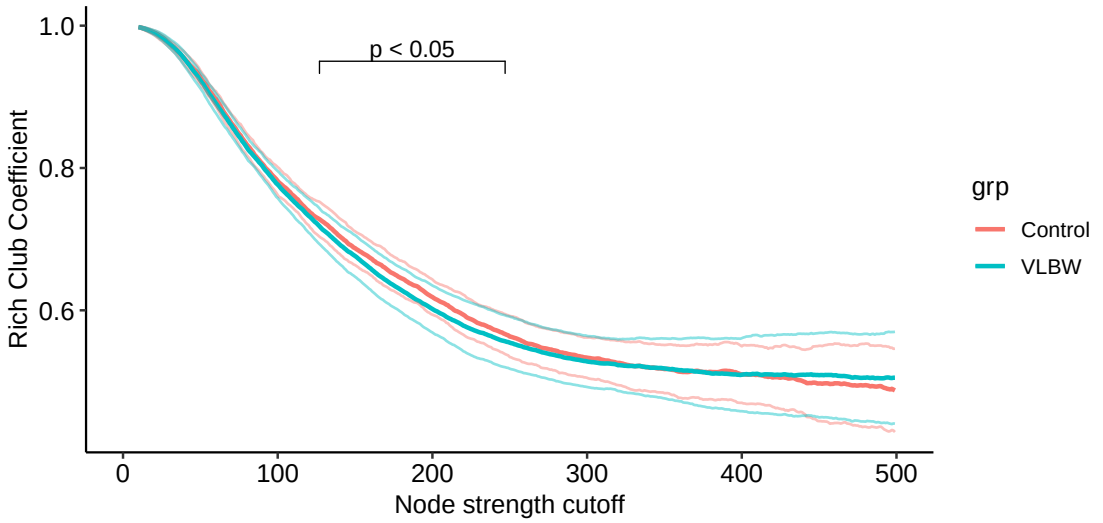

Figure 15: Rich club curve using node strength as the rich club parameter, r, under NSN. Bold lines show group means, lighter lines show one standard deviation either side. r ranges from zero, including all nodes, to 500, including 5% of nodes. Significant group differences are seen between $r = 127$, 42% of nodes, and $r = 247$, 20% of nodes. These differences do not survive BH FDR correction, but are significantly correlated.

4 Discussion

4.1 Interpretation of results

White matter tracts

Twelve tracts were found to have a significantly smaller volume in the VLBW group compared to controls (table 11). This indicates WM growth remains stunted into early adulthood in several regions. Two tracts, the forceps major (fma) and left temporal cingulum subsection (cbt_l, hippocampal white matter) showed both significantly lower FA and greater MD in the VLBW group. In addition, the right optic radiation (or_r) also showed a significantly greater MD, with a non-significantly lower FA. These results indicate poorer WM health in these tracts for VLBW individuals.

Reduced volumes are consistent with the widespread impairment of WM development seen in literature. Curiously, being born VLBW did not show as strong of an effect on the DTI indicators of microstructural WM health as previous DTI studies through childhood and adolescence. This indicates that WM may eventually mature similarly in VLBW adults as controls, but with a reduced volume.

Various microstructural alterations could give rise to the observed differences in FA and MD in the reported tracts. An important consequence of VP/VLBW birth is the known disruption to process of myelination in the white matter (as per section 1.1). Poorer myelination of these tracts in the VLBW group is a likely underlying cause which would be consistent with the observed differences in FA and MD. Another explanation could be a simple decrease in axon density, which would also be consistent with these results and the altered development following a preterm birth.

Damage to the acoustic radiations is one known mechanism leading to the higher rates of hearing loss seen in VLBW/VP cohorts [Cristobal and Oghalai, 2008]. The smaller volumes of these tracts shown here may be related to the vulnerability of these tracts.

The left cortico-spinal tract and superiorthalamic radiation, shown to have a reduced volume, are both important tracts in the motor network. The differences seen in these tracts are consistent with the poorer motor outcomes seen in VLBW/VP cohorts. A reduction in the left hemisphere in particular is an interesting finding worthy of further investigation given the lateralisation of some language functions.

It is reported that the splenium is a tract critical for reading skills, with damage to the splenium associated with alexia [Dougherty et al., 2005]. A trend of poorer reading ability, but not dyslexia, is observed among VP/VLBW children (age four and nine, [Samuelsson et al., 1999]), but not significantly persisting into adulthood (ages 9 and 15, [Samuelsson et al., 2006]). The reduced volume and integrity of the forceps major, containing the splenium, may be reflective of this trend.

A previous whole-brain analysis performed on this dataset also identified lower FA in the forceps major, but no significant difference in cbt_l, or MD globally. A slightly greater RD, and a mix of increased and decreased AD was found. It is unclear whether the cbt_l and or_r showed significant differences in AD and RD [Pascoe et al., 2019]. Overall, the results presented here show fewer significant differences than the TBSS study, but are consistent with the forceps major.

That analysis was carried out using tract based spatial statistics (TBSS). TBSS provides an

option with which to address registration in diffusion-weighted images; it does so by constructing a WM tract skeleton using the voxels with the greatest FA perpendicular to the skeleton. This takes only the most central voxels along principal WM tracts. The tractographic approach used here seeks to identify complete WM tracts, and compare all voxels in each tract in aggregate. The inclusion of more data beyond the centre of the track may explain slightly discrepancy between results.

Several studies have suggested specific associations of AD and RD to specific microstructural properties. RD was linked to dysmyelination [Song et al., 2002], and AD to axonal injury [Budde et al., 2009]. These relationships are known to perform poorly when axonal damage or loss, inflammation, or demyelination coexist [Winklewski et al., 2018]; or under certain arrangements such as in the crossing fibres problem [Wheeler-Kingshott and Cercignani, 2009]. Given the number of models and comparisons planned, I explicitly decided not to assess AD and RD.

PCA

PCA of FA values from all the reconstructed WM tracts revealed a single principal component with a significant group difference. This component resembled the motor network, with the strong contributions from the cortico-spinal tracts and superior thalamic radiations (left and right), followed by the forceps major and minor. This component is mirrored in the third PC of MD (table 9), with the same four motor tracts. This MD component however did not show a significant group difference. This indicates that these tracts are strongly related to one another, and at lease in terms of FA, showed an association with being born VLBW. It is noteworthy that these tracts are identified bi-latterlly. This indicates that differences in the microstructural properties of these motor tracts were consistent across brain hemispheres, even if the volumes of these tracts were not.

It is less clear which networks the other components found for MD might represent. A few tracts appear bi-laterally, such as the acoustic radiations and vertical occipital fasciculi, but many do not.

Graph properties

Of the integration metrics investigated, the VLBW group has a non-significant decrease in characteristic path length (CPL) relative to controls, and an increase in global efficiency, significant under node strength normalisation. Overall this would indicate that the VLBW group tends to have better global communication than controls.

With CPL bring more influenced by longer paths, and the opposite true for efficiency, we can infer that the longer paths are similar in each group, while the short paths tend to be shorter in the VLBW group. This would give rise to the difference in significance seen between the metrics.

The segregation measures shown in figure: 14 show the VLBW group having both a greater modularity and a lower mean CC when compared to controls. Paradoxically, both of these measures are thought to be measures of network segregation, related to the tendency to form clear sub-groups. A possible solution to this arises when the scale of the modules is considered.

Modularity suffers from a resolution limit, allowing it to only look at modules of a certain size, related to a parameter of the community finding algorithm. With the default value used in this analysis, the vast majority of subjects had four to eight modules found. This gives each module on average 20 to 40 regions, which represent large modular structures. The greater modularity

observed in the VLBW group then indicates an organisation of nodes more naturally forming larger sub-graphs.

The CC inherently looks only at the local neighbourhood of each node by evaluating the tendency for pairs of nodes in the local neighbourhood to be connected. This gives a much finer resolution with which to view network segregation. A high clustering is related to nodes being in a locally integrated, but globally segregated environment.

A simultaneous high modularity and low clustering might then indicate that the VLBW group tends to have stronger community structure on the scale of 20-60 nodes, but fewer or weaker interconnections within those communities.

The per-node CC, seen in figure 17 largely reflects the global difference seen earlier, with a particularly strong effect seen in the central grey matter. The notable exception to this is the clustering within the cerebellum, where overall greater clustering is seen in the VLBW group. The cerebellar increase does not survive FDR correction in most regions, but this would be an interesting point of further investigation. The cerebellum is important for movement and coordination, areas in which VLBW/VP groups often perform poorly. The CC within the cerebellum may be informative of patient outcomes.

Structural network studies of preterm born individuals are largely restricted to the first few months or years after birth [Brown et al., 2014, Thompson et al., 2016]. Furthermore, differences in methodology limit the comparability of studies (as explored below). As such, this analysis represents the only (to the best of our knowledge) graph theoretical analysis of adults born either premature or with VLBW.

4.1.1 Limitations and future direction

As has been stated before, DTI has strong limitations from its gaussian assumptions. An inability to resolve multiple fibre populations, and general oversimplification of the underlying processes restricts our ability to make inferences about the underlying microstructures. Implementing a more complex technique, such as constrained spherical deconvolution (CST), or diffusion kurtosis imaging (DKI) would allow a more precise probe into the cellular arrangement in VLBW brains. CST allows multiple fibre populations to be estimated, at greater angular resolution, but requires scanning with a greater b-value that was acquired for this dataset [Tournier et al., 2007, Wilkins et al., 2015, Dell'Acqua et al., 2013]. DKI allows the skew of the diffusion to be estimated, increasing confidence in the results, but will require additional scans with at lease three (two non-zero) b-values [Steven et al., 2014].

A related limitation arises from the susceptibility artefacts present in DWI. These artefacts, resulting here in an elongation of the frontal lobes, are a well known issue with echo-planar imaging (EPI) used in most diffusion sequences. The direction of elongation/compression is related to the direction of phase encoding. Modern DWI sequences commonly reverse this direction to allow the artefacts to be accurately and quickly corrected for [Andersson et al., 2003, Smith et al., 2004, Graham et al., 2017]. Taking reverse phase encoded images was not commonplace at the time of scanning. Techniques such as FSL's EDDY can partially correct for the distortions without requiring reverse encoded images, but more heavy-handed approaches, such as deep learning algorithms, may be advisable for future analyses [Schilling et al., 2019, Qiao and Shi, 2022]. The small elongations would have affected tractography to a small degree, as the distances

in the anterior and posterior regions would be slightly off. Along with inconsistent distances, the volumes found by XTract would also be affected by these artefacts. This should have the same effect across both VLBWs and controls and so be unlikely to bias these results, but will impact volumetric comparisons to other MRI acquisitions.

A logical next step in the analysis of this data is to incorporate measures relating to neurological outcomes. Associations among WM integrity and both motor and neurocognitive outcomes would provide further understanding of the long-term consequences of VLBW. Furthermore, these brain-behaviour relationships could be compared to previous studies of younger cohorts to elucidate any consistent relationships across development. In particular, it would be interesting to compare those principal components which resembled the motor network to movement and coordination outcomes.

The Xtract reconstruction algorithm failed to identify several tracts, 61 in total. At least one tract failed in 47 of 190 subjects, with at most three tracts failing in each subject, and at least one subject failed in 9 of 42 tracts. The poorest performing tracts were the left and right fornix (16 each), and the superior longitudinal faciculus (9). This was handled by excluding the NaN values from direct comparisons, and interpolating using MICE for PCA. The rate at which this occurred did not vary significantly between groups, so this is not thought to have biased results.

An important source of bias to be aware of in neuroimaging research, is the potential for circular analysis. For example, picking what to investigate based on preliminary results, such as investigating a tract voxelwise based on a whole-tract difference. A subtle variation of this may be at play with the DTI metrics found by XTract. Tractography is based on the DWI; the diffusion properties of each voxel influence its chance of being included in a given tract. The voxels chosen in turn have their diffusion properties analysed. This double-dipping into diffusion properties may potentially bias results, however, further investigation would be needed to determine the extent of this effect.

The graph theoretical analysis completed here is one of the first to analyse the structural connectivity in young adults born VLBW. Several limitations with the current methods have been identified below, in section 4.2. In this exciting, developing field, there is a need for a comprehensive review of the vast methodological differences. These span across scanning protocols, pre-processing, parcellation, tractography, formulation of edge strengths, thresholding, metrics reported and method for calculating them. Understanding how these choices affect results and interpretations is crucial to making valid, meaningful and insightful statements, and designs for future studies.

4.2 Structural network analysis

Brain network analysis offers a truly unique insight into the organisational properties relating to both cognition and clinical practice. This field is still in its infancy, with wild methodological differences between studies. These include parcellations, construction and normalisation of connection matrices, selection of properties, and even how to calculate properties. This makes it difficult to make meaningful comparisons in the literature, as these decisions can null or even reverse trends.

What has been studied here is largely restricted to structural networks, constructed through probabilistic tractography. Here I would like to raise some perceived issues arising from this process, and offer some suggestions to alleviate them.

4.2.1 Normalisation

When probabilistic tractography is run, several outputs can be generated. In this analysis, total streamline count between each pair or regions was used. This has the advantage of making minimal assumptions regarding the underlying processes, but necessitates normalising the connection matrices, as streamline count is proportional to region volume.

In this thesis, two methods have been used: node strength normalisation (NSN), a novel algorithm which scales connection matrices such that the mean edge strength in each subject is one; and waytotal (Wt) normalisation, a standard approach which scales each region to have an efferent strength of one.

Edge strengths under these normalisations are not directly comparable between subjects, as the absolute strengths of each edge is not known. While they may be approximately correct, it is highly unlikely that the strengths should be this way between subjects, especially when the VLBW group is known to be at greater risk of widespread white matter damage.

A difference in absolute scaling is not an issue for some graph properties which only require the relative strength within subjects to be known. This should be considered when selecting metrics. Of the seven metrics calculated here, all but CC are invariant to scaling of the entire connectivity matrix, as per NSN. Unfortunetly, all vary when scaling each node's outgoing strength, as per waytotal normalisation.

Providing this valid basis upon which to compare subjects is the greatest boon to NSN over waytotal normalisation. Furthermore, it allows a meaningful rich club curve to be calculated, without necessitating thresholding of the connectivity matrices.

In terms of performance, NSN was similar to Wt for most metrics. Of the four global metrics, a greater difference was seen in three under NSN, potentially indicating a stronger sensitivity. Betweenness centrality and nodewise clustering generally show a smaller variance under NSN with a similar relative effect size, tentatively indicating better overall accuracy.

The assumption underlting NSN is that the true connectivity matrix is symmetric. This requires both symmetry in the fibre modelling, and in tractography. Diffusion imaging must be symmetric at each voxel, and the ball and stick model used in this analysis retains this symmetry. The paths taken by the streamlines may not be, in the case of converging and diverging tracts. Some exotic tractography techniques, such as those using asymmetric fiber populations [Bastiani et al., 2017], may not be suited to this iteration of NSN. Further research under different tractography algorithms would be advisable to validate its use.

4.2.2 Metrics

Graph measures were introduced in section 2.7.4 and an evaluation of CC, rich club and modularity is given here. Many have a sound foundation for their definition and interpretation in binary graphs, but become muddied or misrepresented by poor generalisations to weighted graphs.

Rich club

The rich club is a commonly observed network feature in which the highly connected nodes preferentially connect to each other. To quantify this property, a rich club coefficient, $\phi(k)$, is calculated. In binary networks, $\phi(k)$ is the proportion of edges present in the subgraph comprising of nodes with degree of at least k, out of the total number of possible edges which could exist in such a subgraph.

Rich club organisation also arises in random networks. The highly connected nodes have more connections, and are therefore more likely to connect with all other nodes, not just those of high degree. Due to this, it is common to normalise by the average rich club coefficient of equivalent random networks when attempting to discern whether the rich club exists. This is not necessary for this analysis, as our groups are being compared relative to each other.

A similar metric is defined for weighted networks, the weighted rich club parameter, $\phi^w(r)$ [Opsahl et al., 2008a]. To select the rich club, nodes are ordered and selected based on a richness parameter, r. All nodes with richness over some threshold for r forms the weighted rich club subgraph. The total strength of edges within this subgraph, $W_{>r}$, is found, along with the total strength of the corresponding number of strongest edges, $\sum_{l=1}^{E_{>r}} w_l^{rank}$, where $E_{>r}$ is the number of edges in the rich club, and w_l^{rank} is the l^{th} strongest edge. The ratio of these gives the weighted rich club coefficient

$$\phi^w(r) = \frac{W_{>r}}{\sum_{l=1}^{E_{>r}} w_l^{rank}}$$

This should perform well, and be faithful to the unweighted case, so long as r is chosen appropriately. Three candidate properties for r were originally investigated: node degree, node strength and average edge strength (totals strength over degree). Average strength is reported to perform the best, as strongly connected nodes are selected, while also accounting for connectedness [Opsahl et al., 2008a].

An important factor when considering which to choose is the impact of noise on $\phi^w(r)$. Edges with no true underlying connectivity are very likely to end up with some small, non-zero strength when probabalistic models are used, as it is here. This drastically inflates node degree, and hence deflates average edge strength. Thresholding can mitigate this problem, but was not done for this analysis due to discarding of information, and difficulties selecting an appropriate threshold. Regardless, metrics should not be reliant on thresholding to delineate weak edges into true and false positives.

The best of these candidates for r may then be node strength. This was used successfully with NSN, producing the rich club curve reported, however, all node strengths are scaled to 1 under waytotal normalisation, making the rich club non-discernable.

Keeping in mind that under NSN, each subject's connection matrix has been scaled to have an average edge strength of one, node strength (used as r) is equivalent to a proportion of average node strength. To demonstrate this mathematically, consider richness as a node strength over r.

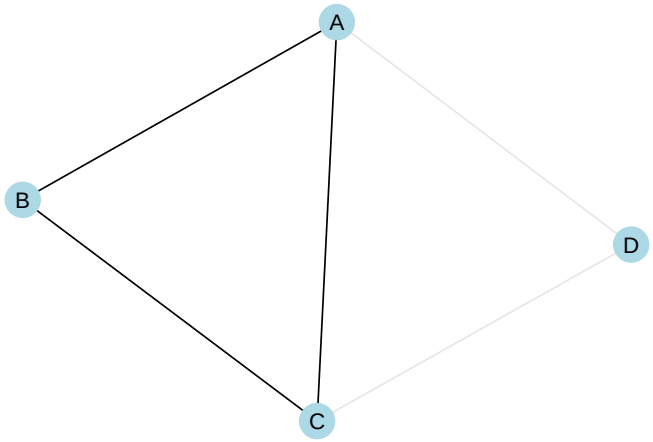

Figure 18: Example graph with strong edges AB, BC and CA; and weak edges AD and DC

Each node has their absolute strength, a_i, scaled to $t_i = \frac{a_i}{\sum_j a_j} n$, where t_i is the NSN strength of the ith node, and n is the number of nodes in the graph. Selecting each $t_i > r$ finds nodes with $\frac{a_i}{\sum_j a_j} > nr$, a proportionate measure. This is advantageous, as it retains the ability to distinguish the rich club, and allows comparisons between subjects. Analyses would benefit from obviating this fact, and scaling to remove n, to allow easier comparisons between studies.

Clustering coefficient

Binary CC, C_i, finds the proportion of a node's neighbours which are connected to each other. Formally,

$$C_i = \frac{2t_i}{k_i(k_i - 1)}$$

where t_i is the number of triangles around node i, doubled as the graphs are undirected, and k_i is the node degree, so $k_i(k_i - 1)$ gives the number of (directed) triplets around node i. This can equally well be considered as the number of times the closed triangle subgraph ($\triangle$) occurs, modulated by occurrences of the open triangle subgraph ($\angle$) around a given node.

It is desirable for generalisations of this to weighted networks to resolve to the binary case as strong edges $\to$1 and weak edges $\to$0. In addition, it would be logical for strong edges to be weighted more than weak edges.

A weighted CC may be calculated in a number of ways (see [Opsahl and Panzarasa, 2009]). The generalisation used in BCT is that proposed by [Onnela et al., 2005], which considers the 'intensity' of the triangular subgraphs around each node. Intensity is defined as the geometric mean of normalised edge weights in the subgraph, $\sum_{j,k} \sqrt[3]{\hat{w}_{ij}\hat{w}_{jk}\hat{w}_{ki}}$ (where $\hat{w}_{ij} = w_{ij}/max(w_{ij})$ is the edge weight from region i to j, scaling the maximum edge strength to 1). The sum of intensities replaces the count of closed triangles in the binary case, giving

$$\widetilde{C}_i = \frac{\sum_{j,k} \sqrt[3]{\hat{w}_{ij}\hat{w}_{jk}\hat{w}_{ki}}}{k_i(k_i - 1)} \tag{11}$$

.

This generalisation only fulfils the requirement of resolving to the binary case as strong edges tend to 1, as the number of open triangles has not been generalised from the binary case. To see this, consider the graph depicted in figure 18: with one strong triangle, ABC, and one weak, ACD. We would expect $\widetilde{C_A}$ to be near one, as D is very weakly connected to A, so ABC, a closed triangle, should contribute the majority to $\widetilde{C_A}$. This is not the case, as each non-zero edge is considered equally important. The one strong closed triangle ABC (and weak closed triangle ACD) gets modulated by the three open triangles BAC, BAD and CAD, giving $\widetilde{C_A} \approx 1/3$. Furthermore, if AD were lowered to zero, $\widetilde{C_A}$ will snap up from 1/3 to 1.

A lesser issue is the choice of geometric mean for defining subgraph intensity. This seems arbitrary beyond fulfilling the desirable property of being 1 only when all values are 1, and dropping to 0 when any value drops to 0. This leads to no clear interpretation in the context of brain networks, though this is by no means the only example of this. Perhaps if edge strength were interpretable as a form of *speed*, the harmonic mean may be appropriate, while also fulfilling the above requirements.

Global clustering coefficient

Global CC is the arithmetic mean of all nodes $\widetilde{C}_i$, and suffers the same issues. In addition, nodes with high strength/degree are weighted equally to those of low degree. This is not necessarily an issue, but it is worth noting that triangles around low degree/strength nodes contribute more to the global CC than triangles around high degree/strength nodes.

Clustering coefficient and thresholding

Where weak, dubious edges strongly affect a metric, such as the diminishing of CC, removing these weak edges by thresholding becomes attractive.

Thresholding was done by removing between none and 90% of the weakest edges. This was performed after the main analysis was carried out, and so is not intended to analyse group differences per se, due to multiple comparisons issues. Instead this was done look into the behaviour of the metrics at hand.

The CC under a varying threshold is shown in figure 19. Overall, CC increased exponentially when thresholding was used. Remarkably this trend was stronger in the VLBW group, leading to a switch in significant differences from a lower CC at low thresholds to higher CC at high thresholds, for VLBWs. This was hypothesised to indicate that the VLBW group tended to have more weak/dubious edges, but the strong edges observed tended to be stronger than the controls. This would result in the observed trend, as the weak edges would dubiously lower CC, but when removed leave a stronger clustering structure.

To test this, the logs of the edge strengths were found, and the ratio of the histograms between groups was plotted (figure 20). We do indeed see a greater spread in the VLBW edge strengths, as shown by their relatively higher frequencies of extreme edge strengths. The change in significance also roughly lines up with the plateau seen in figure 19, though further investigation would be required to confirm this conjecture.

Modularity

Modularity, Q, quantifies the quality of a given modular structure. For binary undirected graphs, it is calculated as the fraction of edges falling within the given groups, less the expected

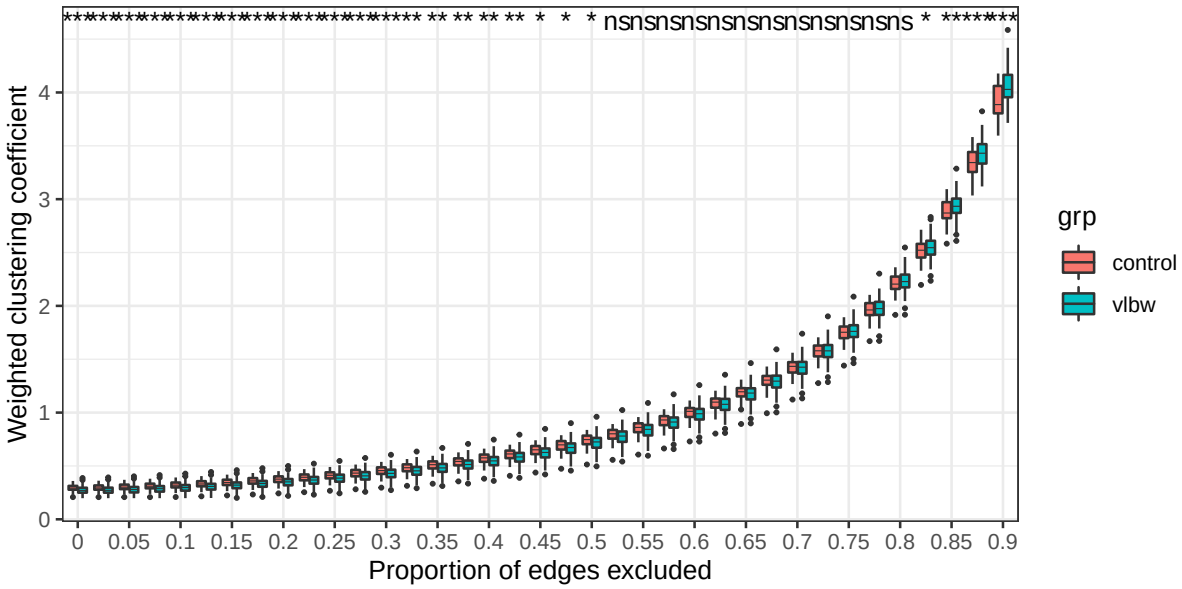

Figure 19: Clustering coefficient for controls and VLBWs (left & right at each threshold) under a varying threshold, under node strength normalisation. Significance levels for the group difference at each threshold are shown near the top. Ns: $p > 0.05$; *: $p \leqslant 0.05$; **: $p \leqslant 0.01$; ***: $p \leqslant 0.001$ (0 to 0.3, 0.875 and 0.9). These group differences are not corrected for age, sex, or multiple comparisons.

fraction for an equivalent random network [Newman and Girvan, 2004]. This captures the idea that a good clustering should have much greater connectivity within groups than we would expect by chance. This ranges from -0.5, indicating only without group edges, to 1, indicating only within group edges. The 'equivalent random network' in this case is the average of graphs with degree, or strength, distribution preserved [**?**].

Modularity suffers from a resolution limit. As proposed groups become smaller, they have an increasingly reduced expected number of edges between them and other groups. For sufficiently small groups, any connection can be seen as a strong indication of connectedness [Fortunato and Barthlemy, 2007].

4.2.3 NSN limitations and future work

In this analysis, I have demonstrated the usefulness of the novel normalisation algorithm NSN in structural network analysis. While results here are promising, further work is required to characterise how noise effects this normalisation. With the output matrix being theoretically symmetric, each element effectively has two estimates, which may allow the underlying uncertainty in T to be estimated. This could be pursued in future work.

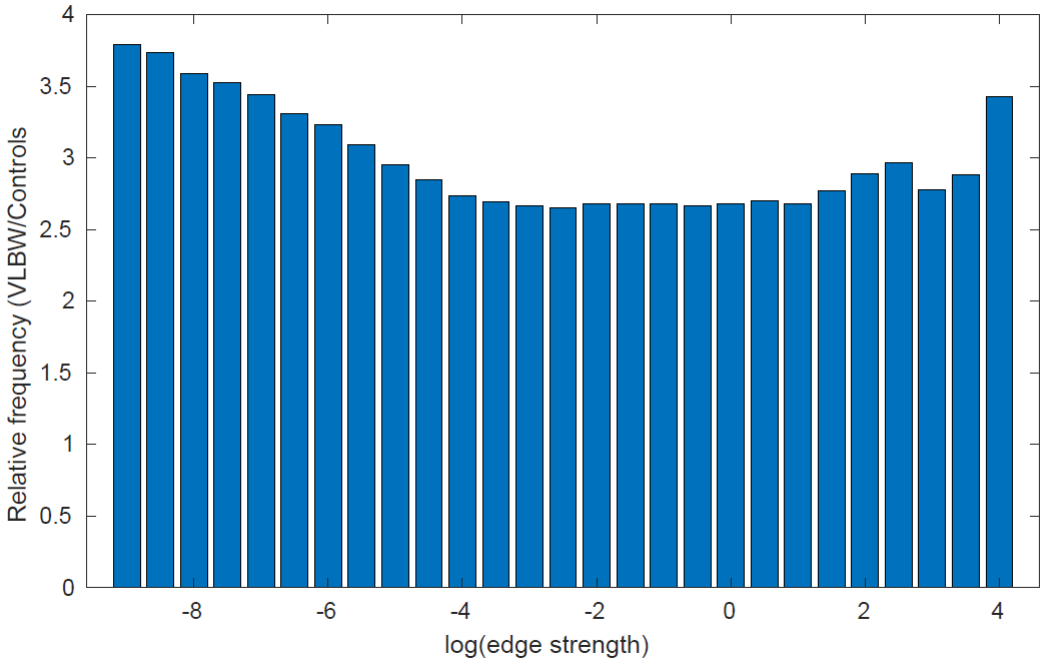

Figure 20: Relative frequencies of edges, binned by edge strength. The non-significant clustering occurs between a log strength of -3.5 and 1

5 Conclusions

Tract-wise analysis used tractography with established masks to isolate whole WM tracts in each individual. This allowed comparisons of DTI measures and volumes for each tract between adults born VLBW and age-matched controls born with normal birthweight. Significantly reduced tract volume in a number of tracts was identified in the VLBW groups, and key tracts showed reduced FA and increased MD. PCA identified interesting patterns of bi-lateral white matter tract differences between the VLBW and healthy control groups.

Structural network analysis used tractography to find the strength of the connections between anatomically distinct regions of GM. This was used to find properties of the structural network topology thought to depict important aspects of organisation, including integration, segregation, hubs and network infrastructure. There was evidence to suggest the VLBW group exhibited a slight increase in integration and segregation on a large scale, but lower segregation on a node-wise scale. Mixed evidence suggests that a select few hub nodes are changed in the VLBW groupp. These differences are shown to persist into adulthood.

A novel algorithm to normalise connection matrices was developed and used alongside the traditional method with the intention of improving the validity of results. Alongside this, a significant amount of work went into understanding and evaluating common methods and metrics in graph theoretical network analysis. It is the hope that this normalisation scheme, and other recommendations made here will find broad applications in brain network analysis improving the validity and interpretability of this field.

Acknowledgements

A huge thank you to Dr Tracy Melzer for your direct supervisory support, which has lifted the quality of my work this past year; and also for squeezing me into an MRI machine after hours.

Thanks also to the wonderful team at NZBRI, for the friendly environment and lunch room banter. Dee for the reliable admin and warm welcomes. Traci for keeping me fueled on more than just beans. Reza for your technical wizardry, and guidance. Will for helping me make sense of neuro-anatomy. The institution as a whole, for access to the building and technology.

Thanks Prof Brian Darlow and Dr Sarah Harris, the previous and current PI of the NZ VLBW study, for data access and guidance, to Prof Lianne Woodward, for the introduction to the field of child development, and to Dr Steven Marsh, for the help wrangling UC's paperwork.

6 Appendix

PC	Tract	(rotation)					
1	af_r (0.21)	ifo_l (0.21)	ifo_r (0.21)	mdlf_l (0.2)	mdlf_r (0.2)	slf3_r (0.2)	af_l (0.19)
2	str_l (-0.32)	cst_l (-0.31)	str_r (-0.3)	cst_r (-0.29)	fma (0.24)	fmi (0.24)	cbp_l (0.21)
3	atr_r (-0.28)	atr_l (-0.28)	fmi (-0.28)	cbp_r (-0.25)	fa_l (-0.24)	ilf_l (0.23)	fa_r (-0.22)
4	fx_l (0.54)	fx_r (0.39)	cbt_r (0.35)	cbt_l (0.33)	vof_r (-0.23)	mcp (0.18)	cbp_l (-0.17)
5	mcp (-0.45)	ar_r (0.36)	slf2_r (-0.35)	ar_l (0.34)	fa_r (-0.28)	uf_l (0.27)	atr_l (0.25)

Table 8: Tracts contributing to the top five components for FA.

PC	Tract	(rotation)					
1	mdlf_l (0.2)	af_l (0.2)	af_r (0.2)	slf3_l (0.2)	ifo_r (0.19)	slf3_r (0.19)	str_r (0.19)
2	or_l (0.31)	or_r (0.3)	fa_l (-0.27)	fa_r (-0.25)	fma (0.25)	fmi (-0.23)	cbt_r (0.23)
3	cbp_l (-0.32)	cbp_r (-0.31)	fmi (-0.29)	cst_r (0.29)	cst_l (0.27)	str_l (0.25)	str_r (0.24)
4	ar_l (-0.39)	fma (0.31)	af_l (-0.29)	ar_r (-0.27)	ilf_l (-0.26)	uf_l (-0.25)	or_r (0.21)
5	vof_l (0.35)	atr_l (-0.33)	cbt_l (-0.26)	vof_r (0.23)	slf3_r (0.23)	fx_l (-0.22)	cbp_r (0.21)

Table 9: Tracts contributing to the top five components for MD.

	Metric	Nrm	$\mu_{Control}$ (σ)	μ_{VLBW} (σ)	$\mu_{VLBW} - \mu_{Control}$ (σ)	t-stat	p-value
1	CPL	Wt	65.7 (5.34e-01)	64.9 (3.09e-01)	7.29e-01 (6.28e-01)	-4.20	4.0e-05
2	CPL	NSN	0.472 (1.04e-02)	0.450 (6.04e-03)	2.13e-02 (1.23e-02)	0.32	7.5e-01
3	GE	Wt	0.0208 (1.58e-04)	0.0211 (9.13e-05)	-3.39e-04 (1.85e-04)	4.70	4.6e-06
4	GE	NSN	4.41 (4.77e-02)	4.7 (2.76e-02)	-2.90e-01 (5.61e-02)	3.40	8.9e-04
5	Mod	Wt	0.431 (4.23e-03)	0.442 (2.45e-03)	-1.17e-02 (4.97e-03)	1.70	9.7e-02
6	Mod	NSN	0.385 (4.00e-03)	0.396 (2.32e-03)	-1.09e-02 (4.71e-03)	1.30	1.8e-01
7	MCC	Wt	0.00155 (2.19e-05)	0.00148 (1.27e-05)	6.32e-05 (2.58e-05)	-3.80	2.0e-04
8	MCC	NSN	0.290 (4.82e-03)	0.274 (2.79e-03)	1.59e-02 (5.66e-03)	-3.90	1.4e-04

Table 10: Statistical comparisons for global graph measures. Values have been corrected for age and sex.

	Tract	$\mu_{Control}$ (SE)	μ_{VLBW} (SE)	$\mu_{(Control-VLBW)}$ (SE)	t-stat	p-value	q-value
1	ac	11527 (990)	10281 (537)	1245 (1162)	-1.071	0.285	0.499
2	af_l	50692 (834)	49414 (453)	1278 (980)	-1.304	0.194	0.387
3	af_r	55113 (894)	54407 (485)	706 (1050)	-0.672	0.502	0.664
4	**ar_l**	6092 (392)	4576 (212)	1516 (460)	-3.294	**0.001**	**0.009**
5	**ar_r**	5344 (342)	3860 (189)	1485 (405)	-3.662	**<0.001**	**0.006**
6	atr_l	35653 (608)	34347 (330)	1306 (715)	-1.828	0.069	0.171
7	atr_r	34297 (590)	33846 (320)	451 (693)	-0.651	0.516	0.664
8	**cbd_l**	16182 (444)	14838 (241)	1345 (521)	-2.580	**0.011**	**0.041**
9	cbd_r	17074 (601)	16460 (326)	614 (706)	-0.870	0.385	0.599
10	cbp_l	2553 (166)	2545 (90)	8 (195)	-0.043	0.966	0.966
11	cbp_r	2677 (167)	2622 (91)	56 (196)	-0.285	0.776	0.815
12	cbt_l	6179 (184)	6082 (100)	96 (217)	-0.446	0.656	0.754
13	cbt_r	5883 (157)	5928 (85)	-45 (184)	0.245	0.807	0.827
14	**cst_l**	25585 (632)	23194 (343)	2391 (742)	-3.224	**0.001**	**0.009**
15	cst_r	26481 (582)	25559 (316)	922 (684)	-1.349	0.179	0.376
16	fa_l	22166 (452)	21246 (245)	920 (531)	-1.733	0.085	0.198
17	fa_r	21046 (469)	21742 (255)	-696 (551)	1.263	0.208	0.397
18	**fma**	41568 (811)	38633 (440)	2935 (953)	-3.081	**0.002**	**0.012**
19	**fmi**	53199 (967)	49900 (525)	3299 (1135)	-2.906	**0.004**	**0.019**
20	fx_l	8673 (507)	7700 (283)	973 (600)	-1.621	0.107	0.236
21	**fx_r**	7006 (421)	5578 (233)	1428 (497)	-2.873	**0.005**	**0.019**
22	ifo_l	55272 (976)	54262 (530)	1010 (1147)	-0.881	0.380	0.599
23	ifo_r	57339 (951)	56354 (516)	985 (1117)	-0.882	0.379	0.599
24	**ilf_l**	30308 (634)	27625 (345)	2683 (745)	-3.601	**<0.001**	**0.006**
25	**ilf_r**	31613 (643)	29149 (349)	2464 (755)	-3.263	**0.001**	**0.009**
26	mcp	33448 (1254)	34693 (681)	-1245 (1473)	0.845	0.399	0.599
27	mdlf_l	40484 (632)	39642 (343)	841 (742)	-1.133	0.259	0.472
28	mdlf_r	41323 (574)	41047 (312)	276 (674)	-0.410	0.682	0.754
29	*or_l*	29170 (543)	27921 (295)	1248 (638)	-1.958	*0.052*	*0.145*
30	*or_r*	31226 (498)	30058 (270)	1168 (584)	-1.998	*0.047*	*0.141*
31	slf1_l	21281 (2009)	20191 (1063)	1090 (2319)	-0.470	0.639	0.754
32	slf1_r	20630 (1961)	21462 (1048)	-832 (2291)	0.363	0.717	0.772
33	slf2_l	17862 (1354)	16639 (748)	1222 (1596)	-0.766	0.445	0.644
34	slf2_r	25028 (1316)	24037 (715)	992 (1545)	-0.642	0.522	0.664
35	**slf3_l**	32653 (942)	28891 (512)	3762 (1107)	-3.400	**0.001**	**0.009**
36	**slf3_r**	35516 (907)	32883 (493)	2633 (1065)	-2.472	**0.014**	**0.050**
37	**str_l**	28089 (485)	26049 (263)	2040 (569)	-3.585	**<0.001**	**0.006**
38	str_r	25806 (460)	24772 (250)	1034 (540)	-1.914	0.057	0.150
39	*uf_l*	23955 (686)	22084 (373)	1871 (806)	-2.321	*0.021*	*0.069*
40	uf_r	19999 (512)	19751 (278)	247 (601)	-0.412	0.681	0.754
41	vof_l	14712 (423)	15037 (230)	-325 (497)	0.653	0.514	0.664
42	vof_r	15539 (419)	15756 (228)	-218 (492)	0.442	0.659	0.754

Table 11: Volumetric statistical comparisons table. Volumes given in mm^3. q-values have undergone FDR correction.

	Tract	$\mu_{Control}$ (SE)	μ_{VLBW} (SE)	$\mu_{(Control-VLBW)}$ (SE)	t-stat	p-value	q-value
1	ac	0.3715 (0.0061)	0.3681 (0.0035)	0.0034 (0.0072)	-0.468	0.640	0.901
2	af_l	0.3401 (0.0027)	0.3440 (0.0016)	-0.0039 (0.0032)	1.218	0.225	0.548
3	af_r	0.3492 (0.0027)	0.3515 (0.0016)	-0.0023 (0.0032)	0.720	0.473	0.827
4	ar_l	0.3542 (0.0055)	0.3653 (0.0031)	-0.0111 (0.0064)	1.729	0.085	0.441
5	*ar_r*	0.3723 (0.0055)	0.3893 (0.0032)	-0.0170 (0.0065)	2.611	*0.010*	0.103
6	atr_l	0.3467 (0.0025)	0.3510 (0.0014)	-0.0044 (0.0029)	1.516	0.131	0.548
7	atr_r	0.3517 (0.0026)	0.3520 (0.0015)	-0.0002 (0.0030)	0.081	0.935	0.945
8	cbd_l	0.3452 (0.0032)	0.3401 (0.0018)	0.0051 (0.0037)	-1.374	0.171	0.548
9	cbd_r	0.3134 (0.0036)	0.3131 (0.0021)	0.0003 (0.0042)	-0.070	0.945	0.945
10	cbp_l	0.3742 (0.0046)	0.3642 (0.0027)	0.0099 (0.0054)	-1.830	0.069	0.414
11	cbp_r	0.3325 (0.0044)	0.3330 (0.0025)	-0.0005 (0.0051)	0.098	0.922	0.945
12	**cbt_l**	0.2605 (0.0036)	0.2458 (0.0021)	0.0147 (0.0043)	-3.428	**0.001**	**0.016**
13	cbt_r	0.2703 (0.0043)	0.2647 (0.0025)	0.0057 (0.0050)	-1.127	0.261	0.548
14	cst_l	0.3937 (0.0036)	0.3947 (0.0021)	-0.0010 (0.0042)	0.225	0.822	0.945
15	cst_r	0.3997 (0.0035)	0.4031 (0.0020)	-0.0034 (0.0041)	0.820	0.413	0.771
16	fa_l	0.3083 (0.0025)	0.3103 (0.0014)	-0.0020 (0.0029)	0.673	0.502	0.843
17	fa_r	0.3165 (0.0027)	0.3170 (0.0015)	-0.0005 (0.0031)	0.156	0.876	0.945
18	**fma**	0.3857 (0.0036)	0.3682 (0.0021)	0.0174 (0.0042)	-4.154	**<0.001**	**0.002**
19	fmi	0.3567 (0.0030)	0.3585 (0.0017)	-0.0018 (0.0035)	0.502	0.616	0.901
20	fx_l	0.2779 (0.0045)	0.2756 (0.0027)	0.0023 (0.0054)	-0.434	0.665	0.901
21	fx_r	0.2712 (0.0044)	0.2743 (0.0026)	-0.0031 (0.0052)	0.591	0.555	0.897
22	ifo_l	0.3630 (0.0024)	0.3607 (0.0014)	0.0023 (0.0028)	-0.804	0.422	0.771
23	ifo_r	0.3734 (0.0025)	0.3700 (0.0015)	0.0034 (0.0030)	-1.135	0.258	0.548
24	ilf_l	0.3387 (0.0030)	0.3398 (0.0017)	-0.0011 (0.0035)	0.322	0.748	0.945
25	ilf_r	0.3514 (0.0034)	0.3508 (0.0019)	0.0006 (0.0040)	-0.158	0.874	0.945
26	mcp	0.3391 (0.0037)	0.3306 (0.0022)	0.0085 (0.0044)	-1.940	0.054	0.414
27	mdlf_l	0.3524 (0.0028)	0.3581 (0.0016)	-0.0056 (0.0033)	1.681	0.094	0.441
28	*mdlf_r*	0.3594 (0.0027)	0.3680 (0.0016)	-0.0086 (0.0032)	2.671	*0.008*	0.103
29	or_l	0.3817 (0.0031)	0.3776 (0.0018)	0.0041 (0.0037)	-1.131	0.260	0.548
30	or_r	0.3872 (0.0031)	0.3825 (0.0018)	0.0046 (0.0037)	-1.257	0.211	0.548
31	slf1_l	0.3409 (0.0051)	0.3521 (0.0028)	-0.0112 (0.0059)	1.898	0.059	0.414
32	slf1_r	0.3448 (0.0049)	0.3514 (0.0028)	-0.0066 (0.0058)	1.139	0.256	0.548
33	slf2_l	0.3237 (0.0042)	0.3295 (0.0025)	-0.0058 (0.0049)	1.180	0.240	0.548
34	slf2_r	0.3281 (0.0035)	0.3299 (0.0020)	-0.0018 (0.0041)	0.443	0.658	0.901
35	slf3_l	0.3150 (0.0028)	0.3194 (0.0016)	-0.0044 (0.0033)	1.339	0.182	0.548
36	slf3_r	0.3244 (0.0026)	0.3230 (0.0015)	0.0014 (0.0031)	-0.459	0.647	0.901
37	str_l	0.3582 (0.0034)	0.3591 (0.0020)	-0.0010 (0.0040)	0.237	0.813	0.945
38	str_r	0.3600 (0.0036)	0.3616 (0.0021)	-0.0016 (0.0042)	0.373	0.709	0.931
39	uf_l	0.3156 (0.0027)	0.3118 (0.0016)	0.0039 (0.0032)	-1.211	0.227	0.548
40	uf_r	0.3153 (0.0029)	0.3125 (0.0017)	0.0028 (0.0034)	-0.813	0.417	0.771
41	vof_l	0.2952 (0.0035)	0.2963 (0.0020)	-0.0011 (0.0041)	0.268	0.789	0.945
42	vof_r	0.3074 (0.0031)	0.3079 (0.0018)	-0.0005 (0.0037)	0.124	0.901	0.945

Table 12: FA statistical comparisons table. q-values have undergone FDR correction.

	Tract	$\mu^{\dagger}_{Control}$ $(SE^{\dagger})$	$\mu^{\dagger}_{VLBW}$ $(SE^{\dagger})$	$\mu^{\dagger}_{(Control-VLBW)}$ $(SE^{\dagger})$	t-stat	p-value	q-value
1	ac	9.3683 (0.1977)	9.6598 (0.1145)	-0.2915 (0.2324)	1.254	0.211	0.411
2	af_l	8.1087 (0.0519)	8.0448 (0.0301)	0.0639 (0.0610)	-1.047	0.296	0.469
3	af_r	7.9741 (0.0481)	7.9020 (0.0278)	0.0721 (0.0565)	-1.276	0.203	0.411
4	*ar_l*	8.5038 (0.0890)	8.2349 (0.0512)	0.2689 (0.1044)	-2.576	*0.011*	0.082
5	*ar_r*	8.1124 (0.0812)	7.8550 (0.0480)	0.2575 (0.0961)	-2.679	*0.008*	0.082
6	atr_l	8.5492 (0.0650)	8.5402 (0.0376)	0.0090 (0.0764)	-0.118	0.906	0.942
7	atr_r	8.5002 (0.0813)	8.6202 (0.0471)	-0.1200 (0.0956)	1.255	0.211	0.411
8	cbd_l	8.0052 (0.0534)	7.9864 (0.0309)	0.0188 (0.0628)	-0.299	0.765	0.846
9	cbd_r	8.2053 (0.0669)	8.3003 (0.0388)	-0.0950 (0.0787)	1.208	0.229	0.418
10	cbp_l	8.1882 (0.0568)	8.2025 (0.0330)	-0.0143 (0.0668)	0.214	0.831	0.895
11	cbp_r	8.1963 (0.0613)	8.2686 (0.0356)	-0.0723 (0.0721)	1.003	0.317	0.469
12	**cbt_l**	9.0848 (0.0961)	9.5136 (0.0556)	-0.4288 (0.1129)	3.797	**<0.001**	**0.007**
13	cbt_r	9.2095 (0.0897)	9.3903 (0.0519)	-0.1808 (0.1054)	1.716	0.088	0.284
14	cst_l	8.4979 (0.0896)	8.7031 (0.0519)	-0.2052 (0.1053)	1.948	0.053	0.222
15	cst_r	8.4313 (0.0856)	8.6047 (0.0496)	-0.1734 (0.1006)	1.723	0.086	0.284
16	fa_l	9.0558 (0.0871)	8.9725 (0.0505)	0.0833 (0.1024)	-0.813	0.417	0.565
17	fa_r	8.9089 (0.0830)	8.8082 (0.0480)	0.1008 (0.0975)	-1.033	0.303	0.469
18	**fma**	8.7090 (0.0907)	9.0967 (0.0525)	-0.3876 (0.1066)	3.637	**<0.000**	**0.007**
19	fmi	8.9288 (0.0719)	8.8099 (0.0416)	0.1189 (0.0845)	-1.408	0.161	0.411
20	fx_l	11.8828 (0.2673)	12.1035 (0.1589)	-0.2208 (0.3167)	0.697	0.487	0.620
21	fx_r	11.8319 (0.2200)	12.1576 (0.1295)	-0.3257 (0.2601)	1.252	0.212	0.411
22	ifo_l	8.0398 (0.0417)	8.0742 (0.0241)	-0.0344 (0.0490)	0.702	0.484	0.620
23	*ifo_r*	7.9518 (0.0454)	8.0701 (0.0263)	-0.1183 (0.0533)	2.219	*0.028*	0.146
24	ilf_l	7.7509 (0.0429)	7.6797 (0.0249)	0.0712 (0.0505)	-1.410	0.160	0.411
25	ilf_r	7.6842 (0.0445)	7.6544 (0.0258)	0.0297 (0.0524)	-0.568	0.571	0.666
26	mcp	7.7955 (0.0594)	7.7265 (0.0344)	0.0690 (0.0698)	-0.989	0.324	0.469
27	mdlf_l	7.9550 (0.0501)	7.9070 (0.0290)	0.0480 (0.0588)	-0.816	0.415	0.565
28	mdlf_r	7.9860 (0.0464)	7.9232 (0.0268)	0.0628 (0.0545)	-1.152	0.251	0.439
29	*or_l*	7.9467 (0.0624)	8.1098 (0.0361)	-0.1631 (0.0734)	2.224	*0.027*	0.146
30	**or_r**	7.9776 (0.0692)	8.2254 (0.0401)	-0.2478 (0.0814)	3.046	**0.003**	**0.037**
31	slf1_l	8.6125 (0.1005)	8.5438 (0.0563)	0.0687 (0.1165)	-0.590	0.556	0.666
32	slf1_r	8.7508 (0.1125)	8.6729 (0.0644)	0.0779 (0.1319)	-0.590	0.556	0.666
33	slf2_l	8.3191 (0.0860)	8.4267 (0.0509)	-0.1075 (0.1016)	1.058	0.291	0.469
34	slf2_r	8.4071 (0.0823)	8.4133 (0.0477)	-0.0062 (0.0968)	0.064	0.949	0.949
35	slf3_l	8.4008 (0.0625)	8.3025 (0.0362)	0.0983 (0.0734)	-1.339	0.182	0.411
36	slf3_r	8.2064 (0.0662)	8.1985 (0.0383)	0.0078 (0.0778)	-0.101	0.920	0.942
37	str_l	8.6975 (0.0898)	8.8439 (0.0520)	-0.1464 (0.1055)	1.387	0.167	0.411
38	*str_r*	8.5494 (0.0938)	8.7729 (0.0543)	-0.2235 (0.1102)	2.028	*0.044*	0.205
39	uf_l	8.7216 (0.0828)	8.5546 (0.0479)	0.1670 (0.0973)	-1.716	0.088	0.284
40	*uf_r*	8.7056 (0.0604)	8.5248 (0.0350)	0.1808 (0.0710)	-2.546	*0.012*	0.082
41	vof_l	7.6719 (0.0622)	7.5809 (0.0360)	0.0910 (0.0732)	-1.243	0.215	0.411
42	vof_r	7.4394 (0.0629)	7.4631 (0.0364)	-0.0237 (0.0739)	0.321	0.749	0.846

Table 13: MD statistical comparisons table. † Values increased by a factor of 10^4 for ease of display. q-values have undergone FDR correction.

References

[FSL,] FSL - FslWiki.

[ICD, 2019] (2019). ICD-10 Version:2019.

[Aanes et al., 2020] Aanes, S., Bjuland, K. J., Lrum, A. M. W., Weider, S., Evensen, K. A. I., Indredavik, M., Brubakk, A.-M., Hberg, A., Lhaugen, G. C., and Skranes, J. S. (2020). Relationship between hippocampal subfield volumes and memory function in adults born preterm with very low birth weight (VLBW). *Clinical Obstetrics, Gynecology and Reproductive Medicine*. Accepted: 2021-02-17T10:58:27Z Publisher: OA Text.

[Agrawal et al., 2018] Agrawal, S., Rao, S. C., Bulsara, M. K., and Patole, S. K. (2018). Prevalence of Autism Spectrum Disorder in Preterm Infants: A Meta-analysis. *Pediatrics*, 142(3). Publisher: American Academy of Pediatrics.

[Alamolhoda et al., 2021] Alamolhoda, S. H., Haghdoost, S., Shariatifar, N., Zare, E., and Ahmadi Doulabi, M. (2021). Risk of Child ADHD and Low Birth Weight: A Systematic Review Study. *International Journal of Pediatrics*, 9(9):14421–14434. Publisher: Mashhad University of Medical Sciences.

[Alexander et al., 2007] Alexander, A. L., Lee, J. E., Lazar, M., and Field, A. S. (2007). Diffusion tensor imaging of the brain. *Neurotherapeutics*, 4(3):316–329.

[Andersen, 2003] Andersen, S. L. (2003). Trajectories of brain development: point of vulnerability or window of opportunity? *Neuroscience & Biobehavioral Reviews*, 27(1):3–18.

[Andersson et al., 2007a] Andersson, J. L., Jenkinson, M., and Smith, S. (2007a). Non-linear registration, aka Spatial normalisation FMRIB technical report TR07JA2. *FMRIB Analysis Group of the University of Oxford*, 2(1):e21.

[Andersson et al., 2007b] Andersson, J. L. R., Jenkinson, M., and Smith, S. (2007b). Non-linear optimisation FMRIB Technial Report TR07JA1.

[Andersson et al., 2003] Andersson, J. L. R., Skare, S., and Ashburner, J. (2003). How to correct susceptibility distortions in spin-echo echo-planar images: application to diffusion tensor imaging. *NeuroImage*, 20(2):870–888.

[Andersson and Sotiropoulos, 2016] Andersson, J. L. R. and Sotiropoulos, S. N. (2016). An integrated approach to correction for off-resonance effects and subject movement in diffusion MR imaging. *NeuroImage*, 125:1063–1078.

[Arima and Fukuoka, 2020] Arima, Y. and Fukuoka, H. (2020). Developmental origins of health and disease theory in cardiology. *Journal of Cardiology*, 76(1):14–17.

[Arnaud et al., 2007] Arnaud, C., Daubisse-Marliac, L., White-Koning, M., Pierrat, V., Larroque, B., Grandjean, H., Alberge, C., Marret, S., Burguet, A., Ancel, P.-Y., Supernant,

K., and Kaminski, M. (2007). Prevalence and Associated Factors of Minor Neuromotor Dysfunctions at Age 5 Years in Prematurely Born Children: The EPIPAGE Study. *Archives of Pediatrics & Adolescent Medicine*, 161(11):1053–1061.

[Back, 2014] Back, S. A. (2014). Cerebral white and gray matter injury in newborns: New insights into pathophysiology and management. *Clinics in perinatology*, 41(1):1–24.

[Ballabh and de Vries, 2021] Ballabh, P. and de Vries, L. S. (2021). White matter injury in infants with intraventricular haemorrhage: mechanisms and therapies. *Nature reviews. Neurology*, 17(4):199–214.

[Bastiani et al., 2017] Bastiani, M., Cottaar, M., Dikranian, K., Ghosh, A., Zhang, H., Alexander, D. C., Behrens, T. E., Jbabdi, S., and Sotiropoulos, S. N. (2017). Improved tractography using asymmetric fibre orientation distributions. *NeuroImage*, 158:205–218.

[Beaulieu, 2002] Beaulieu, C. (2002). The basis of anisotropic water diffusion in the nervous system a technical review. *NMR in Biomedicine*, 15(7-8):435–455. _eprint: https://onlinelibrary.wiley.com/doi/pdf/10.1002/nbm.782.

[Beaulieu and Allen, 1994] Beaulieu, C. and Allen, P. S. (1994). Water diffusion in the giant axon of the squid: Implications for diffusion-weighted MRI of the nervous system. *Magnetic Resonance in Medicine*, 32(5):579–583. _eprint: https://onlinelibrary.wiley.com/doi/pdf/10.1002/mrm.1910320506.

[Behrens et al., 2007] Behrens, T. E. J., Berg, H. J., Jbabdi, S., Rushworth, M. F. S., and Woolrich, M. W. (2007). Probabilistic diffusion tractography with multiple fibre orientations: What can we gain? *NeuroImage*, 34(1):144–155.

[Behrens et al., 2003] Behrens, T. E. J., Woolrich, M. W., Jenkinson, M., Johansen-Berg, H., Nunes, R. G., Clare, S., Matthews, P. M., Brady, J. M., and Smith, S. M. (2003). Characterization and propagation of uncertainty in diffusion-weighted MR imaging. *Magnetic Resonance in Medicine*, 50(5):1077–1088.

[Besson et al., 2014] Besson, P., Dinkelacker, V., Valabregue, R., Thivard, L., Leclerc, X., Baulac, M., Sammler, D., Colliot, O., Lehricy, S., Samson, S., and Dupont, S. (2014). Structural connectivity differences in left and right temporal lobe epilepsy. *NeuroImage*, 100:135–144.

[Blondel et al., 2008] Blondel, V. D., Guillaume, J.-L., Lambiotte, R., and Lefebvre, E. (2008). Fast unfolding of communities in large networks. *Journal of statistical mechanics: theory and experiment*, 2008(10):P10008.

[Bolk et al., 2018] Bolk, J., Farooqi, A., Hafstrm, M., den, U., and Serenius, F. (2018). Developmental Coordination Disorder and Its Association With Developmental Comorbidities at 6.5 Years in Apparently Healthy Children Born Extremely Preterm. *JAMA pediatrics*, 172(8):765–774.

[Bonilha et al., 2012] Bonilha, L., Nesland, T., Martz, G. U., Joseph, J. E., Spampinato, M. V., Edwards, J. C., and Tabesh, A. (2012). Medial temporal lobe epilepsy is associated with neuronal fibre loss and paradoxical increase in structural connectivity of limbic structures. *Journal of Neurology, Neurosurgery, and Psychiatry*, 83(9):903–909.

[Bosma et al., 2009] Bosma, I., Reijneveld, J. C., Klein, M., Douw, L., van Dijk, B. W., Heimans, J. J., and Stam, C. J. (2009). Disturbed functional brain networks and neurocognitive function in low-grade glioma patients: a graph theoretical analysis of resting-state MEG. *Nonlinear Biomedical Physics*, 3(1):9.

[Breeman et al., 2016] Breeman, L. D., Jaekel, J., Baumann, N., Bartmann, P., and Wolke, D. (2016). Attention problems in very preterm children from childhood to adulthood: the Bavarian Longitudinal Study. *Journal of Child Psychology and Psychiatry*, 57(2):132–140. _eprint: https://onlinelibrary.wiley.com/doi/pdf/10.1111/jcpp.12456.

[Brown et al., 2014] Brown, C. J., Miller, S. P., Booth, B. G., Andrews, S., Chau, V., Poskitt, K. J., and Hamarneh, G. (2014). Structural network analysis of brain development in young preterm neonates. *NeuroImage*, 101:667–680.

[Budde et al., 2009] Budde, M. D., Xie, M., Cross, A. H., and Song, S.-K. (2009). Axial Diffusivity Is the Primary Correlate of Axonal Injury in the Experimental Autoimmune Encephalomyelitis Spinal Cord: A Quantitative Pixelwise Analysis. *Journal of Neuroscience*, 29(9):2805–2813.

[Buuren and Groothuis-Oudshoorn, 2011] Buuren, S. v. and Groothuis-Oudshoorn, K. (2011). mice: Multivariate Imputation by Chained Equations in R. *Journal of Statistical Software*, 45:1–67.

[Buxhoeveden and Casanova, 2002] Buxhoeveden, D. P. and Casanova, M. F. (2002). The minicolumn hypothesis in neuroscience. *Brain*, 125(5):935–951.

[Cai et al., 2019] Cai, S., Thompson, D. K., Anderson, P. J., and Yang, J. Y.-M. (2019). Short- and Long-Term Neurodevelopmental Outcomes of Very Preterm Infants with Neonatal Sepsis: A Systematic Review and Meta-Analysis. *Children*, 6(12):131. Number: 12 Publisher: Multidisciplinary Digital Publishing Institute.

[Cald et al., 2006] Cald, X., Narberhaus, A., Junqu, C., Gimnez, M., Vendrell, P., Bargall, N., Segarra, D., and Botet, F. (2006). Corpus Callosum Size and Neuropsychologic Impairment in Adolescents who Were Born Preterm. *Journal of Child Neurology*, 21(5):406–410. Publisher: SAGE Publications Inc.

[Chawanpaiboon et al., 2019] Chawanpaiboon, S., Vogel, J. P., Moller, A.-B., Lumbiganon, P., Petzold, M., Hogan, D., Landoulsi, S., Jampathong, N., Kongwattanakul, K., Laopaiboon, M., Lewis, C., Rattanakanokchai, S., Teng, D. N., Thinkhamrop, J., Watananirun, K., Zhang, J., Zhou, W., and Glmezoglu, A. M. (2019). Global, regional, and national estimates of levels of preterm birth in 2014: a systematic review and modelling analysis. *The Lancet Global Health*, 7(1):e37–e46. Publisher: Elsevier.

[Collins et al., 2018] Collins, A., Weitkamp, J.-H., and Wynn, J. L. (2018). Why are preterm newborns at increased risk of infection? *Archives of disease in childhood. Fetal and neonatal edition*, 103(4):F391–F394.

[Constable et al., 2008] Constable, R. T., Ment, L. R., Vohr, B. R., Kesler, S. R., Fulbright, R. K., Lacadie, C., Delancy, S., Katz, K. H., Schneider, K. C., Schafer, R. J., and others (2008). Prematurely born children demonstrate white matter microstructural differences at 12 years of age, relative to term control subjects: an investigation of group and gender effects. *Pediatrics*, 121(2):306–316. Publisher: American Academy of Pediatrics.

[Cosgrove et al., 2007] Cosgrove, K. P., Mazure, C. M., and Staley, J. K. (2007). Evolving Knowledge of Sex Differences in Brain Structure, Function and Chemistry. *Biological psychiatry*, 62(8):847–855.

[Cristobal and Oghalai, 2008] Cristobal, R. and Oghalai, J. S. (2008). Hearing loss in children with very low birth weight: current review of epidemiology and pathophysiology. *Archives of disease in childhood. Fetal and neonatal edition*, 93(6):F462–F468.

[Crump et al., 2011] Crump, C., Sundquist, K., Winkleby, M. A., and Sundquist, J. (2011). Preterm birth and risk of epilepsy in Swedish adults. *Neurology*, 77(14):1376–1382. Publisher: Wolters Kluwer Health, Inc. on behalf of the American Academy of Neurology Section: Articles.

[Cruz et al., 2005] Cruz, L., Buldyrev, S. V., Peng, S., Roe, D. L., Urbanc, B., Stanley, H. E., and Rosene, D. L. (2005). A statistically based density map method for identification and quantification of regional differences in microcolumnarity in the monkey brain. *Journal of Neuroscience Methods*, 141(2):321–332.

[Darlow et al., 1997] Darlow, B., Horwood, L., Mogridge, N., and Clemett, R. (1997). Prospective study of New Zealand very low birthweight infants: Outcome at 78 years. *Journal of Paediatrics and Child Health*, 33(1):47–51. _eprint: https://onlinelibrary.wiley.com/doi/pdf/10.1111/j.1440-1754.1997.tb00990.x.

[Darlow, 1988] Darlow, B. A. (1988). Incidence of retinopathy of prematurity in New Zealand. *Archives of Disease in Childhood*, 63(9):1083–1086. Publisher: BMJ Publishing Group Ltd Section: Research Article.

[Darlow et al., 2013] Darlow, B. A., Horwood, L. J., Pere-Bracken, H. M., and Woodward, L. J. (2013). Psychosocial Outcomes of Young Adults Born Very Low Birth Weight. *Pediatrics*, 132(6):e1521–e1528. Publisher: American Academy of Pediatrics Section: Article.

[Darlow et al., 2015] Darlow, B. A., Horwood, L. J., Woodward, L. J., Elliott, J. M., Troughton, R. W., Elder, M. J., Epton, M. J., Stanton, J. D., Swanney, M. P., Keenan, R., Melzer, T. R., McKelvey, V. A., Levin, K., Meeks, M. G., Espiner, E. A., Cameron, V. A., and Martin, J. (2015). The New Zealand 1986 very low birth weight cohort as young adults: mapping the road ahead. *BMC Pediatrics*, 15(1):90.

[Dell'Acqua et al., 2013] Dell'Acqua, F., Simmons, A., Williams, S. C., and Catani, M. (2013). Can spherical deconvolution provide more information than fiber orientations? Hindrance modulated orientational anisotropy, a true-tract specific index to characterize white matter diffusion. *Human Brain Mapping*, 34(10):2464–2483. _eprint: https://onlinelibrary.wiley.com/doi/pdf/10.1002/hbm.22080.

[Destrieux et al., 2010] Destrieux, C., Fischl, B., Dale, A., and Halgren, E. (2010). Automatic parcellation of human cortical gyri and sulci using standard anatomical nomenclature. *NeuroImage*, 53(1):1–15.

[Disselhoff et al., 2020] Disselhoff, V., Jakab, A., Schnider, B., Latal, B., Wehrle, F. M., and Hagmann, C. F. (2020). Inhibition is associated with whole-brain structural brain connectivity on network level in school-aged children born very preterm and at term. *NeuroImage*, 218:116937.

[Dong and Yu, 2011] Dong, Y. and Yu, J.-L. (2011). An overview of morbidity, mortality and long-term outcome of late preterm birth. *World Journal of Pediatrics*, 7(3):199.

[Douaud et al., 2009] Douaud, G., Behrens, T. E., Poupon, C., Cointepas, Y., Jbabdi, S., Gaura, V., Golestani, N., Krystkowiak, P., Verny, C., Damier, P., Bachoud-Lvi, A.-C., Hantraye, P., and Remy, P. (2009). In vivo evidence for the selective subcortical degeneration in Huntington's disease. *NeuroImage*, 46(4):958–966.

[Dougherty et al., 2005] Dougherty, R. F., Ben-Shachar, M., Deutsch, G., Potanina, P., Bammer, R., and Wandell, B. A. (2005). Occipital-Callosal Pathways in Children: Validation and Atlas Development. *Annals of the New York Academy of Sciences*, 1064(1):98–112. _eprint: https://onlinelibrary.wiley.com/doi/pdf/10.1196/annals.1340.017.

[Edgin et al., 2008] Edgin, J. O., Inder, T. E., Anderson, P. J., Hood, K. M., Clark, C. a. C., and Woodward, L. J. (2008). Executive functioning in preschool children born very preterm: Relationship with early white matter pathology. *Journal of the International Neuropsychological Society*, 14(1):90–101. Publisher: Cambridge University Press.

[Eikenes et al., 2011] Eikenes, L., Lhaugen, G. C., Brubakk, A.-M., Skranes, J., and Hberg, A. K. (2011). Young adults born preterm with very low birth weight demonstrate widespread white matter alterations on brain DTI. *NeuroImage*, 54(3):1774–1785.

[Engel et al., 2013] Engel, J., Thompson, P. M., Stern, J. M., Staba, R. J., Bragin, A., and Mody, I. (2013). Connectomics and epilepsy. *Current opinion in neurology*, 26(2):186–194.

[Englander et al., 2013] Englander, Z. A., Pizoli, C. E., Batrachenko, A., Sun, J., Worley, G., Mikati, M. A., Kurtzberg, J., and Song, A. W. (2013). Diffuse reduction of white matter connectivity in cerebral palsy with specific vulnerability of long range fiber tracts. *NeuroImage: Clinical*, 2:440–447.

[Evensen et al., 2020] Evensen, K. A. I., Ustad, T., Tikanmki, M., Haaramo, P., and Kajantie, E. (2020). Long-term motor outcomes of very preterm and/or very low birth weight individuals

without cerebral palsy: A review of the current evidence. *Seminars in Fetal and Neonatal Medicine*, 25(3):101116.

[Fortunato and Barthlemy, 2007] Fortunato, S. and Barthlemy, M. (2007). Resolution limit in community detection. *Proceedings of the National Academy of Sciences*, 104(1):36–41. Publisher: National Academy of Sciences Section: Physical Sciences.

[Franz et al., 2018] Franz, A. P., Bolat, G. U., Bolat, H., Matijasevich, A., Santos, I. S., Silveira, R. C., Procianoy, R. S., Rohde, L. A., and Moreira-Maia, C. R. (2018). Attention-Deficit/Hyperactivity Disorder and Very Preterm/Very Low Birth Weight: A Meta-analysis. *Pediatrics*, 141(1). Publisher: American Academy of Pediatrics.

[Freeman, 1977] Freeman, L. C. (1977). A Set of Measures of Centrality Based on Betweenness. *Sociometry*, 40(1):35–41. Publisher: [American Sociological Association, Sage Publications, Inc.].

[Gimnez et al., 2006] Gimnez, M., Junqu, C., Narberhaus, A., Bargall, N., Botet, F., and Mercader, J. M. (2006). White matter volume and concentration reductions in adolescents with history of very preterm birth: A voxel-based morphometry study. *NeuroImage*, 32(4):1485–1498.

[Graham et al., 2017] Graham, M. S., Drobnjak, I., Jenkinson, M., and Zhang, H. (2017). Quantitative assessment of the susceptibility artefact and its interaction with motion in diffusion MRI. *PloS One*, 12(10):e0185647.

[Grant and Griffin, 2018] Grant, L. A. and Griffin, N. (2018). *Grainger & allison's diagnostic radiology essentials*. Elsevier Health Sciences.

[Harsan et al., 2007] Harsan, L. A., Poulet, P., Guignard, B., Parizel, N., Skoff, R. P., and Ghandour, M. S. (2007). Astrocytic hypertrophy in dysmyelination influences the diffusion anisotropy of white matter. *Journal of Neuroscience Research*, 85(5):935–944. _eprint: https://onlinelibrary.wiley.com/doi/pdf/10.1002/jnr.21201.

[He et al., 2018] He, L., Li, H., Holland, S. K., Yuan, W., Altaye, M., and Parikh, N. A. (2018). Early prediction of cognitive deficits in very preterm infants using functional connectome data in an artificial neural network framework. *NeuroImage. Clinical*, 18:290–297.

[He and Evans, 2010] He, Y. and Evans, A. (2010). Graph theoretical modeling of brain connectivity. *Current opinion in neurology*, 23(4):341–350.

[Hedrich et al., 2017] Hedrich, T., Pellegrino, G., Kobayashi, E., Lina, J. M., and Grova, C. (2017). Comparison of the spatial resolution of source imaging techniques in high-density EEG and MEG. *NeuroImage*, 157:531–544.

[Herculano-Houzel, 2009] Herculano-Houzel, S. (2009). The Human Brain in Numbers: A Linearly Scaled-up Primate Brain. *Frontiers in Human Neuroscience*, 3:31.

[Himpens et al., 2008] Himpens, E., Van den Broeck, C., Oostra, A., Calders, P., and Vanhaesebrouck, P. (2008). Prevalence, type, distribution, and severity of cerebral palsy in relation to gestational age: a meta-analytic review. *Developmental Medicine & Child Neurology*, 50(5):334–340. _eprint: https://onlinelibrary.wiley.com/doi/pdf/10.1111/j.1469-8749.2008.02047.x.

[Hirvonen et al., 2017] Hirvonen, M., Ojala, R., Korhonen, P., Haataja, P., Eriksson, K., Gissler, M., Luukkaala, T., and Tammela, O. (2017). The incidence and risk factors of epilepsy in children born preterm: A nationwide register study. *Epilepsy Research*, 138:32–38.

[Hollanders et al., 2019] Hollanders, J. J., Schafer, N., van der Pal, S. M., Oosterlaan, J., Rotteveel, J., Finken, M. J. J., and onbehalfoftheDutchPOPS-19CollaborativeStudyGroup (2019). Long-Term Neurodevelopmental and Functional Outcomes of Infants Born Very Preterm and/or with a Very Low Birth Weight. *Neonatology*, 115(4):310–319.

[Jaekel et al., 2013] Jaekel, J., Wolke, D., and Bartmann, P. (2013). Poor attention rather than hyperactivity/impulsivity predicts academic achievement in very preterm and full-term adolescents. *Psychological Medicine*, 43(1):183–196. Publisher: Cambridge University Press.

[Jbabdi et al., 2012] Jbabdi, S., Sotiropoulos, S. N., Savio, A. M., Graa, M., and Behrens, T. E. J. (2012). Model-based analysis of multishell diffusion MR data for tractography: how to get over fitting problems. *Magnetic Resonance in Medicine*, 68(6):1846–1855.

[Jenkinson et al., 2002] Jenkinson, M., Bannister, P., Brady, M., and Smith, S. (2002). Improved Optimization for the Robust and Accurate Linear Registration and Motion Correction of Brain Images. *NeuroImage*, 17(2):825–841.

[Jenkinson and Smith, 2001] Jenkinson, M. and Smith, S. (2001). A global optimisation method for robust affine registration of brain images. *Medical Image Analysis*, 5(2):143–156.

[Jiang et al., 2021] Jiang, H., Liu, H., Huang, T., Wu, L., Wu, F., Liu, C., Wang, M., Jin, C., Yang, J., and Li, X. (2021). Structural network performance for early diagnosis of spastic cerebral palsy in periventricular white matter injury. *Brain Imaging and Behavior*, 15(2):855–864.

[Jones, 2000] Jones, E. G. (2000). Microcolumns in the cerebral cortex. *Proceedings of the National Academy of Sciences of the United States of America*, 97(10):5019–5021.

[Kanel et al., 2021] Kanel, D., Counsell, S. J., and Nosarti, C. (2021). Advances in functional and diffusion neuroimaging research into the long-term consequences of very preterm birth. *Journal of Perinatology*, 41(4):689–706. Number: 4 Publisher: Nature Publishing Group.

[Kassambara and Mundt, 2020] Kassambara, A. and Mundt, F. (2020). factoextra: Extract and visualize the results of multivariate data analyses. manual.

[Kelly et al.,] Kelly, C. E., Harding, R., Lee, K. J., Pascoe, L., Josev, E. K., Spencer-Smith, M. M., Adamson, C., Beare, R., Nosarti, C., Roberts, G., Doyle, L. W.,

Seal, M. L., Thompson, D. K., and Anderson, P. J. Investigating the brain structural connectome following working memory training in children born extremely preterm or extremely low birth weight. *Journal of Neuroscience Research*, n/a(n/a). _eprint: https://onlinelibrary.wiley.com/doi/pdf/10.1002/jnr.24818.

[Khwaja and Volpe, 2008] Khwaja, O. and Volpe, J. J. (2008). Pathogenesis of cerebral white matter injury of prematurity. *Archives of Disease in Childhood - Fetal and Neonatal Edition*, 93(2):F153–F161. Publisher: BMJ Publishing Group Section: Review.

[Kidokoro et al., 2013] Kidokoro, H., Neil, J. J., and Inder, T. E. (2013). New MR Imaging Assessment Tool to Define Brain Abnormalities in Very Preterm Infants at Term. *American Journal of Neuroradiology*, 34(11):2208–2214. Publisher: American Journal of Neuroradiology Section: Pediatrics.

[Kocak, 2009] Kocak, M. (2009). Advanced imaging in paediatric neuroradiology. *Pediatric Radiology*, 39(3):456–463.

[Kramer and Cash, 2012] Kramer, M. A. and Cash, S. S. (2012). Epilepsy as a disorder of cortical network organization. *The Neuroscientist: A Review Journal Bringing Neurobiology, Neurology and Psychiatry*, 18(4):360–372.

[Larvaron et al., 2007] Larvaron, P., Boespflug-Tanguy, O., Renou, J.-P., and Bonny, J.-M. (2007). In vivo analysis of the post-natal development of normal mouse brain by DTI. *NMR in Biomedicine*, 20(4):413–421. _eprint: https://onlinelibrary.wiley.com/doi/pdf/10.1002/nbm.1082.

[Li et al., 2014] Li, H., Xue, Z., Ellmore, T. M., Frye, R. E., and Wong, S. T. C. (2014). Network-based analysis reveals stronger local diffusion-based connectivity and different correlations with oral language skills in brains of children with high functioning autism spectrum disorders. *Human Brain Mapping*, 35(2):396–413. _eprint: https://onlinelibrary.wiley.com/doi/pdf/10.1002/hbm.22185.

[Limperopoulos et al., 2008] Limperopoulos, C., Bassan, H., Sullivan, N. R., Soul, J. S., Robertson, Jr, R. L., Moore, M., Ringer, S. A., Volpe, J. J., and du Plessis, A. J. (2008). Positive Screening for Autism in Ex-preterm Infants: Prevalence and Risk Factors. *Pediatrics*, 121(4):758–765.

[Mandy and Nyirenda, 2018] Mandy, M. and Nyirenda, M. (2018). Developmental Origins of Health and Disease: the relevance to developing nations. *International Health*, 10(2):66–70.

[McCrea and Ment, 2008] McCrea, H. J. and Ment, L. R. (2008). The Diagnosis, Management and Postnatal Prevention of Intraventricular Hemorrhage in the Preterm Neonate. *Clinics in perinatology*, 35(4):777–vii.

[Mikula, 2016] Mikula, S. (2016). Progress Towards Mammalian Whole-Brain Cellular Connectomics. *Frontiers in Neuroanatomy*, 0. Publisher: Frontiers.

[Mori and Zhang, 2006] Mori, S. and Zhang, J. (2006). Principles of Diffusion Tensor Imaging and Its Applications to Basic Neuroscience Research. *Neuron*, 51(5):527–539.

[Mullen et al., 2011] Mullen, K. M., Vohr, B. R., Katz, K. H., Schneider, K. C., Lacadie, C., Hampson, M., Makuch, R. W., Reiss, A. L., Constable, R. T., and Ment, L. R. (2011). Preterm birth results in alterations in neural connectivity at age 16 years. *NeuroImage*, 54(4):2563–2570.

[Murray et al., 2014] Murray, A. L., Scratch, S. E., Thompson, D. K., Inder, T. E., Doyle, L. W., Anderson, J. F. I., and Anderson, P. J. (2014). Neonatal Brain Pathology Predicts Adverse Attention and Processing Speed Outcomes in Very Preterm and/or Very Low Birth Weight Children. *Neuropsychology*, 28(4):552–562.

[Newman and Girvan, 2004] Newman, M. E. J. and Girvan, M. (2004). Finding and evaluating community structure in networks. *Physical Review E*, 69(2):026113. Publisher: American Physical Society.

[Nosarti et al., 2008] Nosarti, C., Giouroukou, E., Healy, E., Rifkin, L., Walshe, M., Reichenberg, A., Chitnis, X., Williams, S. C. R., and Murray, R. M. (2008). Grey and white matter distribution in very preterm adolescents mediates neurodevelopmental outcome. *Brain*, 131(1):205–217.

[Onnela et al., 2005] Onnela, J.-P., Saramki, J., Kertsz, J., and Kaski, K. (2005). Intensity and coherence of motifs in weighted complex networks. *Physical Review E*, 71(6):065103. Publisher: American Physical Society.

[Opsahl et al., 2008a] Opsahl, T., Colizza, V., Panzarasa, P., and Ramasco, J. (2008a). Phys. Rev. Lett. 101, 168702 (2008) - Prominence and Control: The Weighted Rich-Club Effect.

[Opsahl et al., 2008b] Opsahl, T., Colizza, V., Panzarasa, P., and Ramasco, J. J. (2008b). Prominence and Control: The Weighted Rich-Club Effect. *Physical Review Letters*, 101(16):168702. Publisher: American Physical Society.

[Opsahl and Panzarasa, 2009] Opsahl, T. and Panzarasa, P. (2009). Clustering in weighted networks. *Social Networks*, 31(2):155–163.

[Pannek et al., 2014] Pannek, K., Boyd, R. N., Fiori, S., Guzzetta, A., and Rose, S. E. (2014). Assessment of the structural brain network reveals altered connectivity in children with unilateral cerebral palsy due to periventricular white matter lesions. *NeuroImage: Clinical*, 5:84–92.

[Parikh, 2016] Parikh, N. A. (2016). Advanced neuroimaging and its role in predicting neurodevelopmental outcomes in very preterm infants. *Seminars in Perinatology*, 40(8):530–541.

[Park and Friston, 2013] Park, H.-J. and Friston, K. (2013). Structural and functional brain networks: from connections to cognition. *Science (New York, N.Y.)*, 342(6158):1238411.

[Partridge et al., 2004] Partridge, S. C., Mukherjee, P., Henry, R. G., Miller, S. P., Berman, J. I., Jin, H., Lu, Y., Glenn, O. A., Ferriero, D. M., Barkovich, A. J., and Vigneron, D. B. (2004). Diffusion tensor imaging: serial quantitation of white matter tract maturity in premature newborns. *NeuroImage*, 22(3):1302–1314.

[Pascoe et al., 2019] Pascoe, M. J., Melzer, T. R., Horwood, L. J., Woodward, L. J., and Darlow, B. A. (2019). Altered grey matter volume, perfusion and white matter integrity in very low birthweight adults. *NeuroImage. Clinical*, 22:101780.

[Patel, 2016] Patel, R. M. (2016). Short- and Long-Term Outcomes for Extremely Preterm Infants. *American Journal of Perinatology*, 33(3):318–328. Publisher: Thieme Medical Publishers.

[Pedersen, 2020] Pedersen, T. L. (2020). tidygraph: A tidy API for graph manipulation. manual.

[Pedersen, 2021] Pedersen, T. L. (2021). ggraph: An implementation of grammar of graphics for graphs and networks. manual.

[Pierpaoli et al., 2001] Pierpaoli, C., Barnett, A., Pajevic, S., Chen, R., Penix, L. R., Virta, A., and Basser, P. (2001). Water diffusion changes in Wallerian degeneration and their dependence on white matter architecture. *NeuroImage*, 13(6 Pt 1):1174–1185.

[Poduslo and Jang, 1984] Poduslo, S. E. and Jang, Y. (1984). Myelin development in infant brain. *Neurochemical Research*, 9(11):1615–1626.

[Qi et al., 2015] Qi, S., Meesters, S., Nicolay, K., Romeny, B. M. t. H., and Ossenblok, P. (2015). The influence of construction methodology on structural brain network measures: A review. *Journal of Neuroscience Methods*, 253:170–182.

[Qiao and Shi, 2022] Qiao, Y. and Shi, Y. (2022). Unsupervised Deep Learning for FOD-Based Susceptibility Distortion Correction in Diffusion MRI. *IEEE Transactions on Medical Imaging*, 41(5):1165–1175. Conference Name: IEEE Transactions on Medical Imaging.

[R Core Team, 2022] R Core Team (2022). R: A language and environment for statistical computing. manual, Vienna, Austria. tex.organization: R Foundation for Statistical Computing.

[Ray et al., 2014] Ray, S., Miller, M., Karalunas, S., Robertson, C., Grayson, D. S., Cary, R. P., Hawkey, E., Painter, J. G., Kriz, D., Fombonne, E., Nigg, J. T., and Fair, D. A. (2014). Structural and functional connectivity of the human brain in autism spectrum disorders and attention-deficit/hyperactivity disorder: A rich club-organization study. *Human Brain Mapping*, 35(12):6032–6048. Publisher: Wiley-Liss Inc.

[Robinson et al., 2022] Robinson, R., Girchenko, P., Pulakka, A., Heinonen, K., Lhdepuro, A., Lahti-Pulkkinen, M., Hovi, P., Tikanmki, M., Bartmann, P., Lano, A., Doyle, L. W., Anderson, P. J., Cheong, J. L. Y., Darlow, B. A., Woodward, L. J., Horwood, L. J., Indredavik, M. S., Evensen, K. A. I., Marlow, N., Johnson, S., de Mendonca, M. G., Kajantie, E., Wolke, D., and Rikknen, K. (2022). ADHD symptoms and diagnosis in adult preterms: systematic review,

IPD meta-analysis, and register-linkage study. *Pediatric Research*, pages 1–11. Publisher: Nature Publishing Group.

[Rogers and Hintz, 2016] Rogers, E. E. and Hintz, S. R. (2016). Early neurodevelopmental outcomes of extremely preterm infants. *Seminars in Perinatology*, 40(8):497–509.

[Rolls et al., 2020] Rolls, E. T., Huang, C.-C., Lin, C.-P., Feng, J., and Joliot, M. (2020). Automated anatomical labelling atlas 3. *NeuroImage*, 206:116189.

[RStudio Team, 2022] RStudio Team (2022). RStudio: Integrated development environment for R. manual, Boston, MA. tex.organization: RStudio, PBC.

[Rubinov and Sporns, 2010] Rubinov, M. and Sporns, O. (2010). Complex network measures of brain connectivity: Uses and interpretations. *NeuroImage*, 52(3):1059–1069.

[Samuelsson et al., 1999] Samuelsson, S., Bylund, B., Cervin, T., Finnstrm, O., Gddlin, P.-O., Leijon, I., Mrd, S., Rnnberg, J., Sandstedt, P., and Wrngrd, O. (1999). The prevalence of reading disabilities among very-low-birthweight children at 9 years of agedyslexics or poor readers? *Dyslexia*, 5(2):94–112. _eprint: https://onlinelibrary.wiley.com/doi/pdf/10.1002/%28SICI%291099-0909%28199906%295%3A2%3C94%3A%3AAID-DYS135%3E3.0.CO%3B2-N.

[Samuelsson et al., 2006] Samuelsson, S., Finnstrm, O., Flodmark, O., Gddlin, P.-O., Leijon, I., and Wadsby, M. (2006). A longitudinal study of reading skills among very-low-birthweight children: is there a catch-up? *Journal of Pediatric Psychology*, 31(9):967–977.

[Schilling et al., 2019] Schilling, K. G., Blaber, J., Huo, Y., Newton, A., Hansen, C., Nath, V., Shafer, A. T., Williams, O., Resnick, S. M., Rogers, B., Anderson, A. W., and Landman, B. A. (2019). Synthesized b0 for diffusion distortion correction (Synb0-DisCo). *Magnetic Resonance Imaging*, 64:62–70.

[Sejnowski, 2016] Sejnowski, T. J. (2016). Nanoconnectomics. In Kennedy, H., Van Essen, D. C., and Christen, Y., editors, *Micro-, Meso- and Macro-Connectomics of the Brain*. Springer, Cham (CH).

[Shah et al., 2008] Shah, D. K., Doyle, L. W., Anderson, P. J., Bear, M., Daley, A. J., Hunt, R. W., and Inder, T. E. (2008). Adverse neurodevelopment in preterm infants with postnatal sepsis or necrotizing enterocolitis is mediated by white matter abnormalities on magnetic resonance imaging at term. *The Journal of Pediatrics*, 153(2):170–175, 175.e1.

[Skranes et al., 2007] Skranes, J., Vangberg, T. R., Kulseng, S., Indredavik, M. S., Evensen, K. A. I., Martinussen, M., Dale, A. M., Haraldseth, O., and Brubakk, A.-M. (2007). Clinical findings and white matter abnormalities seen on diffusion tensor imaging in adolescents with very low birth weight. *Brain*, 130(3):654–666.

[Smith et al., 2020] Smith, D. D., Sagaram, D., Miller, R., and Gyamfi-Bannerman, C. (2020). Risk of cerebral palsy by gestational age among pregnancies at-risk for preterm birth. 33(12):2059–2063.

[Smith et al., 2004] Smith, S. M., Jenkinson, M., Woolrich, M. W., Beckmann, C. F., Behrens, T. E. J., Johansen-Berg, H., Bannister, P. R., De Luca, M., Drobnjak, I., Flitney, D. E., Niazy, R. K., Saunders, J., Vickers, J., Zhang, Y., De Stefano, N., Brady, J. M., and Matthews, P. M. (2004). Advances in functional and structural MR image analysis and implementation as FSL. *NeuroImage*, 23 Suppl 1:S208–219.

[Song et al., 2002] Song, S.-K., Sun, S.-W., Ramsbottom, M. J., Chang, C., Russell, J., and Cross, A. H. (2002). Dysmyelination revealed through MRI as increased radial (but unchanged axial) diffusion of water. *NeuroImage*, 17(3):1429–1436.

[Soria-Pastor et al., 2008] Soria-Pastor, S., Gimenez, M., Narberhaus, A., Falcon, C., Botet, F., Bargallo, N., Mercader, J. M., and Junque, C. (2008). Patterns of cerebral white matter damage and cognitive impairment in adolescents born very preterm. *International Journal of Developmental Neuroscience*, 26(7):647–654.

[Sporns, 2011] Sporns, O. (2011). The human connectome: a complex network. *Annals of the New York Academy of Sciences*, 1224:109–125.

[Sporns et al., 2005] Sporns, O., Tononi, G., and Ktter, R. (2005). The Human Connectome: A Structural Description of the Human Brain. *PLOS Computational Biology*, 1(4):e42. Publisher: Public Library of Science.

[Stam, 2010] Stam, C. J. (2010). Characterization of anatomical and functional connectivity in the brain: A complex networks perspective. *International Journal of Psychophysiology*, 77(3):186–194.

[Stephens et al., 2012] Stephens, B. E., Bann, C. M., Watson, V. E., Sheinkopf, S. J., Peralta-Carcelen, M., Bodnar, A., Yolton, K., Goldstein, R. F., Dusick, A. M., Wilson-Costello, D. E., Acarregui, M. J., Pappas, A., Adams-Chapman, I., McGowan, E. C., Heyne, R. J., Hintz, S. R., Ehrenkranz, R. A., Fuller, J., Das, A., Higgins, R. D., Vohr, B. R., and Network, f. t. E. K. S. N. I. o. C. H. a. H. D. N. R. (2012). Screening for Autism Spectrum Disorders in Extremely Preterm Infants. *Journal of Developmental & Behavioral Pediatrics*, 33(7):535–541.

[Steven et al., 2014] Steven, A. J., Zhuo, J., and Melhem, E. R. (2014). Diffusion Kurtosis Imaging: An Emerging Technique for Evaluating the Microstructural Environment of the Brain. *American Journal of Roentgenology*, 202(1):W26–W33.

[Su et al., 2016] Su, Y.-Y., Wang, S.-H., Chou, H.-C., Chen, C.-Y., Hsieh, W.-S., Tsao, P.-N., Tsou, K.-I., and Taiwan Premature Infant Follow-up Network (2016). Morbidity and mortality of very low birth weight infants in Taiwan-Changes in 15 years: A population based study. *Journal of the Formosan Medical Association = Taiwan Yi Zhi*, 115(12):1039–1045.

[Takahashi et al., 2002] Takahashi, M., Hackney, D. B., Zhang, G., Wehrli, S. L., Wright, A. C., O'Brien, W. T., Uematsu, H., Wehrli, F. W., and Selzer, M. E. (2002). Magnetic resonance microimaging of intraaxonal water diffusion in live excised lamprey spinal cord. *Proceedings of the National Academy of Sciences*, 99(25):16192–16196. Publisher: National Academy of Sciences Section: Biological Sciences.

[Taylor et al., 2011] Taylor, H. G., Filipek, P. A., Juranek, J., Bangert, B., Minich, N., and Hack, M. (2011). Brain Volumes in Adolescents With Very Low Birth Weight: Effects on Brain Structure and Associations With Neuropsychological Outcomes. *Developmental Neuropsychology*, 36(1):96–117. Publisher: Routledge _eprint: https://doi.org/10.1080/87565641.2011.540544.

[Thompson et al., 2016] Thompson, D. K., Chen, J., Beare, R., Adamson, C. L., Ellis, R., Ahmadzai, Z. M., Kelly, C. E., Lee, K. J., Zalesky, A., Yang, J. Y. M., Hunt, R. W., Cheong, J. L. Y., Inder, T. E., Doyle, L. W., Seal, M. L., and Anderson, P. J. (2016). Structural connectivity relates to perinatal factors and functional impairment at 7years in children born very preterm. *NeuroImage*, 134:328–337.

[Tournier et al., 2007] Tournier, J.-D., Calamante, F., and Connelly, A. (2007). Robust determination of the fibre orientation distribution in diffusion MRI: Non-negativity constrained super-resolved spherical deconvolution. *NeuroImage*, 35(4):1459–1472.

[Tyszka et al., 2006] Tyszka, J. M., Readhead, C., Bearer, E. L., Pautler, R. G., and Jacobs, R. E. (2006). Statistical diffusion tensor histology reveals regional dysmyelination effects in the shiverer mouse mutant. *NeuroImage*, 29(4):1058–1065.

[Tzourio-Mazoyer et al., 2002] Tzourio-Mazoyer, N., Landeau, B., Papathanassiou, D., Crivello, F., Etard, O., Delcroix, N., Mazoyer, B., and Joliot, M. (2002). Automated anatomical labeling of activations in SPM using a macroscopic anatomical parcellation of the MNI MRI single-subject brain. *NeuroImage*, 15(1):273–289.

[van den Heuvel et al., 2017] van den Heuvel, M. P., de Lange, S. C., Zalesky, A., Seguin, C., Yeo, B. T. T., and Schmidt, R. (2017). Proportional thresholding in resting-state fMRI functional connectivity networks and consequences for patient-control connectome studies: Issues and recommendations. *NeuroImage*, 152:437–449.

[van den Heuvel and Sporns, 2013] van den Heuvel, M. P. and Sporns, O. (2013). Network hubs in the human brain. *Trends in Cognitive Sciences*, 17(12):683–696.

[van Diessen et al., 2015] van Diessen, E., Numan, T., van Dellen, E., van der Kooi, A. W., Boersma, M., Hofman, D., van Lutterveld, R., van Dijk, B. W., van Straaten, E. C. W., Hillebrand, A., and Stam, C. J. (2015). Opportunities and methodological challenges in EEG and MEG resting state functional brain network research. *Clinical Neurophysiology*, 126(8):1468–1481.

[Vogel et al., 2018] Vogel, J. P., Chawanpaiboon, S., Moller, A.-B., Watananirun, K., Bonet, M., and Lumbiganon, P. (2018). The global epidemiology of preterm birth. *Best Practice & Research Clinical Obstetrics & Gynaecology*, 52:3–12.

[Vollmer et al., 2017] Vollmer, B., Lundequist, A., Mrtensson, G., Nagy, Z., Lagercrantz, H., Smedler, A.-C., and Forssberg, H. (2017). Correlation between white matter microstructure and executive functions suggests early developmental influence on long fibre tracts in preterm born adolescents. *PLOS ONE*, 12(6):e0178893. Publisher: Public Library of Science.

[Volpe, 2008a] Volpe, J. J. (2008a). Neurology of the newborn E-book. Publisher: Elsevier Health Sciences.

[Volpe, 2008b] Volpe, J. J. (2008b). Postnatal Sepsis, Necrotizing Entercolitis, and the Critical Role of Systemic Inflammation in White Matter Injury in Premature Infants. *The Journal of pediatrics*, 153(2):160–163.

[Volpe, 2009] Volpe, J. J. (2009). The Encephalopathy of PrematurityBrain Injury and Impaired Brain Development Inextricably Intertwined. *Seminars in Pediatric Neurology*, 16(4):167–178.

[Wadhwa et al., 2009] Wadhwa, P. D., Buss, C., Entringer, S., and Swanson, J. M. (2009). Developmental Origins of Health and Disease: Brief History of the Approach and Current Focus on Epigenetic Mechanisms. *Seminars in Reproductive Medicine*, 27(5):358–368. Publisher: Thieme Medical Publishers.

[Wang et al., 2011] Wang, J.-H., Zuo, X.-N., Gohel, S., Milham, M. P., Biswal, B. B., and He, Y. (2011). Graph Theoretical Analysis of Functional Brain Networks: Test-Retest Evaluation on Short- and Long-Term Resting-State Functional MRI Data. *PLOS ONE*, 6(7):e21976. Publisher: Public Library of Science.

[Ward and Beachy, 2003] Ward, R. M. and Beachy, J. C. (2003). Neonatal complications following preterm birth. *BJOG: An International Journal of Obstetrics & Gynaecology*, 110(s20):8–16. _eprint: https://obgyn.onlinelibrary.wiley.com/doi/pdf/10.1046/j.1471-0528.2003.00012.x.

[Warrington et al., 2020] Warrington, S., Bryant, K. L., Khrapitchev, A. A., Sallet, J., Charquero-Ballester, M., Douaud, G., Jbabdi, S., Mars, R. B., and Sotiropoulos, S. N. (2020). XTRACT - Standardised protocols for automated tractography in the human and macaque brain. *NeuroImage*, 217:116923.

[Welton et al., 2015] Welton, T., Kent, D. A., Auer, D. P., and Dineen, R. A. (2015). Reproducibility of Graph-Theoretic Brain Network Metrics: A Systematic Review. *Brain Connectivity*, 5(4):193–202.

[Wheeler-Kingshott and Cercignani, 2009] Wheeler-Kingshott, C. A. and Cercignani, M. (2009). About axial and radial diffusivities. *Magnetic Resonance in Medicine*, 61(5):1255–1260. _eprint: https://onlinelibrary.wiley.com/doi/pdf/10.1002/mrm.21965.

[Wickham, 2016] Wickham, H. (2016). *ggplot2: Elegant graphics for data analysis*. Springer-Verlag New York.

[Wickham et al., 2022] Wickham, H., Franois, R., Henry, L., and Mller, K. (2022). dplyr: A grammar of data manipulation. manual.

[Wickham and Girlich, 2022] Wickham, H. and Girlich, M. (2022). tidyr: Tidy messy data. manual.

[Wilkins et al., 2015] Wilkins, B., Lee, N., Gajawelli, N., Law, M., and Lepor, N. (2015). Fiber estimation and tractography in diffusion MRI: Development of simulated brain images and comparison of multi-fiber analysis methods at clinical b-values. *NeuroImage*, 109:341–356.

[Winklewski et al., 2018] Winklewski, P. J., Sabisz, A., Naumczyk, P., Jodzio, K., Szurowska, E., and Szarmach, A. (2018). Understanding the Physiopathology Behind Axial and Radial Diffusivity ChangesWhat Do We Know? *Frontiers in Neurology*, 9.

[Yamasaki et al., 2017] Yamasaki, T., Maekawa, T., Fujita, T., and Tobimatsu, S. (2017). Connectopathy in Autism Spectrum Disorders: A Review of Evidence from Visual Evoked Potentials and Diffusion Magnetic Resonance Imaging. *Frontiers in Neuroscience*, 0. Publisher: Frontiers.

[Zalesky et al., 2010] Zalesky, A., Fornito, A., Harding, I. H., Cocchi, L., Ycel, M., Pantelis, C., and Bullmore, E. T. (2010). Whole-brain anatomical networks: Does the choice of nodes matter? *NeuroImage*, 50(3):970–983.